



AFRL-AFOSR-VA-TR-2017-0022

Compliant Nanospring Interfaces

Ioannis Chasiotis
UNIVERSITY OF ILLINOIS CHAMPAIGN
506 S WRIGHT ST 364 HENRY ADMIN BLD
URBANA, IL 61801-3620

01/26/2017
Final Report

DISTRIBUTION A: Distribution approved for public release.

Air Force Research Laboratory
AF Office Of Scientific Research (AFOSR)/RTB2

REPORT DOCUMENTATION PAGE			Form Approved OMB No. 0704-0188		
<p>The public reporting burden for this collection of information is estimated to average 1 hour per response, including the time for reviewing instructions, searching existing data sources, gathering and maintaining the data needed, and completing and reviewing the collection of information. Send comments regarding this burden estimate or any other aspect of this collection of information, including suggestions for reducing the burden, to Department of Defense, Executive Services, Directorate (0704-0188). Respondents should be aware that notwithstanding any other provision of law, no person shall be subject to any penalty for failing to comply with a collection of information if it does not display a currently valid OMB control number.</p> <p>PLEASE DO NOT RETURN YOUR FORM TO THE ABOVE ORGANIZATION.</p>					
1. REPORT DATE (DD-MM-YYYY) 26-01-2017		2. REPORT TYPE Final Performance		3. DATES COVERED (From - To) 27 Mar 2013 to 30 Sep 2016	
4. TITLE AND SUBTITLE Compliant Nanospring Interfaces			5a. CONTRACT NUMBER		
			5b. GRANT NUMBER FA9550-13-1-0149		
			5c. PROGRAM ELEMENT NUMBER 61102F		
6. AUTHOR(S) Ioannis Chasiotis			5d. PROJECT NUMBER		
			5e. TASK NUMBER		
			5f. WORK UNIT NUMBER		
7. PERFORMING ORGANIZATION NAME(S) AND ADDRESS(ES) UNIVERSITY OF ILLINOIS CHAMPAIGN 506 S WRIGHT ST 364 HENRY ADMIN BLD URBANA, IL 61801-3620 US			8. PERFORMING ORGANIZATION REPORT NUMBER		
9. SPONSORING/MONITORING AGENCY NAME(S) AND ADDRESS(ES) AF Office of Scientific Research 875 N. Randolph St. Room 3112 Arlington, VA 22203			10. SPONSOR/MONITOR'S ACRONYM(S) AFRL/AFOSR RTB2		
			11. SPONSOR/MONITOR'S REPORT NUMBER(S) AFRL-AFOSR-VA-TR-2017-0022		
12. DISTRIBUTION/AVAILABILITY STATEMENT A DISTRIBUTION UNLIMITED: PB Public Release					
13. SUPPLEMENTARY NOTES					
14. ABSTRACT <p>This research program investigated the mechanics of thin films comprised of dense arrays of 10-micron high Cu and Si micro and nanosprings fabricated as multifunctional compliant interfaces via Glancing Angle Deposition (GLAD). The Cu spring films had 10 coil turns and were deposited with 2000 nm, 2400 nm, 2800 nm, or 3200 nm seed spacing on Si wafers as well as on unseeded Si substrates. Larger seed spacing resulted in Cu springs with larger coil diameter and larger wire thickness. Compression tests were conducted with stress amplitudes between 5 MPa and 50 MPa. At 5 MPa, the compressive stiffness of Cu films was between 1842 and 35315 MPa, with larger values corresponding to larger seed spacing. Notably, the Cu spring films showed no permanent deformation until 20 MPa, when they experienced only 2% permanent strain. The shear stiffness of Cu films was between 21837 and 32285 MPa with unseeded films being the most compliant. Seeding resulted in a weaker interface with the substrate, while unseeded Cu spring films had significant shear strength averaging 160.9 MPa. The normal and shear stiffness values of Cu spring films were several orders of magnitude smaller than bulk Cu and they could be designed to be independent of each other, as opposed to bulk Cu.</p>					
15. SUBJECT TERMS Multifunctional Design, Interface Mechanics, Nanospring					
16. SECURITY CLASSIFICATION OF:		17. LIMITATION OF ABSTRACT	18. NUMBER OF	Standard Form 298 (Rev. 8/98) Prescribed by ANSI Std. Z39.18	

DISTRIBUTION A: Distribution approved for public release.

a. REPORT	b. ABSTRACT	c. THIS PAGE	UU	PAGES	19a. NAME OF RESPONSIBLE PERSON LEE, BYUNG
Unclassified	Unclassified	Unclassified			19b. TELEPHONE NUMBER <i>(Include area code)</i> 703-696-8483



**UNIVERSITY OF ILLINOIS
AEROSPACE ENGINEERING**



**Final Performance Report
Reporting Period: 4/01/2013 - 9/30/2016**

Compliant Nanospring Interfaces

PI: Ioannis Chasiotis

Aerospace Engineering
University of Illinois at Urbana-Champaign
Talbot Lab, 104 S. Wright Street, Urbana, IL 61801
Telephone: (217) 244-1474, Fax: (217) 244-0720, E-mail: chasioti@illinois.edu

**AFOSR Grant # FA9550-13-1-0149
Program Manager: Dr. B.L. "Les" Lee**

January 22, 2017

ACKNOWLEDGEMENTS

The PI and his graduate students gratefully acknowledge the support by the Air Force Office of Scientific Research (AFOSR) through grant FA9550-13-1-0149 with Dr. B.L. Lee as the program manager. We also wish to thank Prof. M. Brett from the University of Alberta for his input in the fabrication of the GLAD films.

ABSTRACT

This research program investigated the mechanics of thin films comprised of dense arrays of 10-micron high Cu and Si micro and nanosprings fabricated as multifunctional compliant interfaces via Glancing Angle Deposition (GLAD). The Cu spring films had 10 coil turns and were deposited with 2000 nm, 2400 nm, 2800 nm, or 3200 nm seed spacing on Si wafers as well as on unseeded Si substrates. Larger seed spacing resulted in Cu springs with larger coil diameter and larger wire thickness. Compression tests were conducted with stress amplitudes between 5 MPa and 50 MPa. At 5 MPa, the compressive stiffness of Cu films was between 184 ± 2 and 353 ± 15 MPa, with larger values corresponding to larger seed spacing. Notably, the Cu spring films showed no permanent deformation until 20 MPa, when they experienced only 2% permanent strain. The shear stiffness of Cu films was between 218 ± 37 and 322 ± 85 MPa with unseeded films being the most compliant. Seeding resulted in a weaker interface with the substrate, while unseeded Cu spring films had significant shear strength averaging 16 ± 0.9 MPa. The normal and shear stiffness values of Cu spring films were several orders of magnitude smaller than bulk Cu and they could be designed to be independent of each other, as opposed to bulk Cu.

Similarly, 10-micron thick Si films comprised of individual springs with 4 or 10 coil turns and seed spacings of 900 nm or 1500 nm were subjected to tension/compression and shear. At 0.5 MPa normal stress, the Si films had compressive stiffness between 26 ± 0.4 and 44 ± 0.9 MPa, while the permanent strain was at most 6.5%. Compared to seeded films, unseeded films had quite reduced compressive stiffness but equivalent or higher shear stiffness. The shear stiffness of the various types of Si spring films was between 7 ± 0.6 and 27 ± 7 MPa, namely ~4 orders of magnitude smaller than solid Si. Microscale uniaxial tension/compression and bending tests of individual Si springs, carried out with a MEMS-based apparatus, provided the properties of individual springs: Springs with 4 coil turns, which had the closest resemblance to ideal open coils, exhibited the smallest axial stiffness values, between 10 and 35 N/m, and the best agreement between film-level stiffness measurements and estimates for the film stiffness based on individual spring stiffness data.

FINAL TECHNICAL REPORT

The objective of this research program was to quantify the enhanced compressive and shear mechanical response of thin films comprised of Cu and Si nanosprings, fabricated by the method of Glancing Angle Deposition (GLAD), as a function of geometrical spring parameters (coil angle, and coil and wire diameters). Furthermore, the mechanical response of individual Si nanosprings was quantified under tension/compression and bending simulating the conditions in which individual springs would be loaded inside films. The two data sets can be used to assess the importance of mechanical interactions of nanosprings in GLAD films.

This Final Progress Report is divided into 4 Sections. The first Section summarizes the state of the art in multifunctional interface films and provides the motivation for this work. The second Section, discusses the experimental procedures that were developed in the course of this program to study interfaces comprised of springs. This is followed by a Section on Results and Discussion, and, finally, a Section on Outlook and Future Work summarizes important directions in this field.

I. MOTIVATION AND RATIONALE

Novel interface materials are expected to provide a spectrum of functionalities, such as enhanced thermal and/or electrical conductivity, resistance to interfacial cracks, high interface compliance between materials with significantly different coefficients of thermal expansion, etc. To this effect, a variety of materials have been explored, such as forests of fibrils, carbon nanotubes (CNTs) and helices [1]. Qu et al. [2] employed films of vertically aligned CNTs as interfaces that can sustain shear strains. A drawback of such films, however, is their weak adhesion, which can be somewhat improved by compression [3]. Similarly, Tong et al. [4] inserted between two surfaces a film of vertical multi-walled CNTs which served as a Thermal Interface Material (TIM), namely as a material with high thermal conductance. The initial thermal conductance was $\sim 10^5$ W/m²K and increased by one order of magnitude by after bonding the multi-walled CNT film with a thin film of indium (In). Kumar et al. [5,6] introduced graphene nanopetals on the surface of nanotubes in CNT arrays, which increased the array stiffness by at least an order of magnitude. The mechanical compliance and recovery upon loading could be increased by growing the CNTs in a helical fashion, thus producing coil-shaped CNTs [7-9]. Finally, Shaddock et al. [10] employed the Glancing Angle Deposition (GLAD) method to directly deposit compliant interfaces between a silicon (Si) surface (e.g. a Si microelectronics chip) and a copper (Cu) film (e.g. a Cu heat sink), achieving thermal resistance as low as ~ 0.01 cm²C/W, which surpasses in performance solutions based on CNTs.

GLAD can produce thin films with slanted, straight, or helical micro- or nano-elements [11-17] by controlling the deposition parameters, such as the rotation speed of the substrate, the deposition rate, the angle between the target and the substrate, and the deposition angle, α . By GLAD, micro- or nanostructures form due to “self-shadowing” owed to the oblique deposition angle of the incident vapor onto a flat surface. Upon formation of random nuclei on a flat surface, the high incident angle of the vapor results in “shadowing” of smaller nuclei, thus halting their growth. As a result, thin films with helical elements are deposited at high deposition angles ($\alpha > 80^\circ$) and at relatively slow substrate rotational speeds (a full rotation of the substrate corresponds to the deposition of one helix turn). Seeding of the substrate prevents random nucleation, therefore, resulting in orderly elements as first shown by Malac et al. [18].

The microstructural intricacies of GLAD films have been shown to provide a multitude of functionalities, such as energy storage and energy harvesting [10,19-24]. However, little is known about their mechanical compliance and robustness. For instance, Seto et al. [25] performed nanoindentation on spring films comprised of silicon monoxide (SiO), titanium (Ti) and chromium (Cr) [26]. The lateral and transverse stiffness of tantalum oxide (Ta₂O₅) spring films with a capping layer was measured by Hirakata et al. [27] and Sumigawa et al. [28]. At the individual spring level, Liu et al. [29] measured the stiffness of single Si springs with an Atomic Force Microscope (AFM). In that work, seeding of the substrate with tungsten (W) posts allowed for deposition of well separated springs without overlap. The measured stiffness of the Si springs was reported to be lower than expected due to the application of off-axis load by the AFM tip. The aforementioned works could not separate the effect of lateral spring interactions which influence the measured spring stiffness [29]. Stiffening due to lateral spring interactions inside films could be evaluated by testing individual springs isolated from GLAD films.

In this research program the mechanical behavior of Si and Cu spring films produced via GLAD was determined under compression via an indenter and in shear with the aid of a

custom-made apparatus. The two types of materials were selected for their multifunctional potential as thermally conductive interfaces between materials with different coefficients of thermal expansion (Cu), and as compliant high surface-to-volume “films” for photovoltaic energy harvesting and Li^+ storage (Si). Figure 1 provides an outline of the experimental methods and approach followed in this research program. 10- μm thick films of Cu and Si springs with two different seed spacings and coil turns per unit length, as well as unseeded films were studied. Their compressive and lateral (shear) stiffness, and permanent deformation were measured at the film level using capped and uncapped films which represent different cases of boundary conditions. At the nanoscale, the mechanical behavior of the individual Si nanosprings, isolated from the same four types of seeded films, was measured in tension, compression and shear (bending) via Microelectromechanical Systems (MEMS) based tools, as shown in Figure 1. The results of single spring experiments provide the basis to understand the spring interactions occurring in film-level compression and shear experiments.

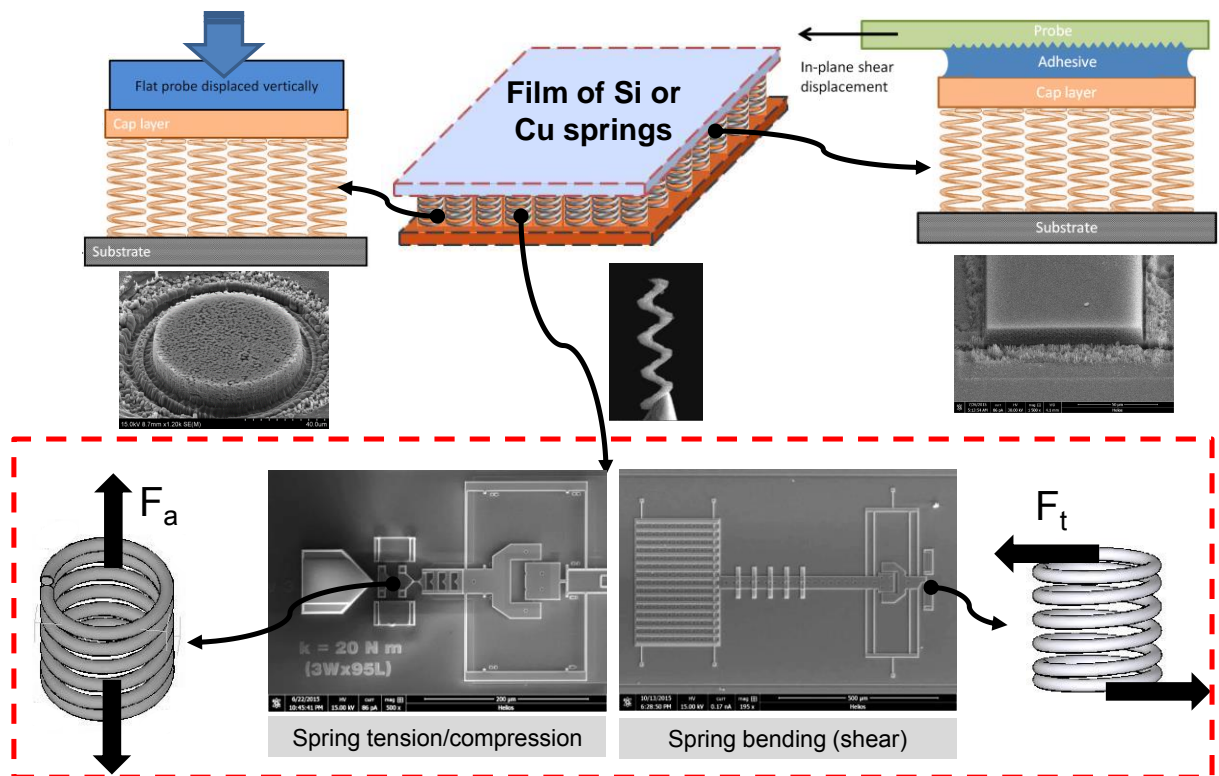


Figure 1. Graphical summary of the experimental approach pursued in this research program.

II. EXPERIMENTAL PROCEDURES

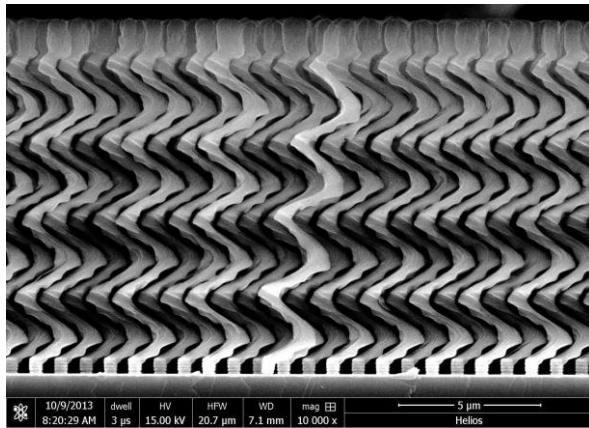
II.1 Fabrication of Si Spring Films

All Si spring films, Figure 2(a-f), were fabricated by GLAD at the commercial foundry of Micralyne, in Edmonton, Canada. Seeded and unseeded Si substrates were tilted at 85° and rotated at constant speed [11,12]. The choice of deposition parameters provided control of the wire diameter, coil diameter, and coil/helix angle. Unseeded films demonstrated a large distribution of wire and coil diameters and resulted in highly intertwined springs, Figure 2(e,f). The increased seed spacing in the case of seeded springs reduced intertwining between adjacent springs, Figure 2(a-d). The seeded Si spring films were fabricated on a Si wafer with a regular pattern of 500 nm tall Si posts that served as seeds with spacing of either 900 nm or 1500 nm. For each seed spacing, Si springs with 1000 nm or 2500 nm pitch height were fabricated, thus resulting in six different types of films, all being 10±0.3µm thick, Figure 2(a-f). Seeding of the Si substrate with 500 nm high Si posts was prepared via Deep Reactive-Ion Etching (DRIE).

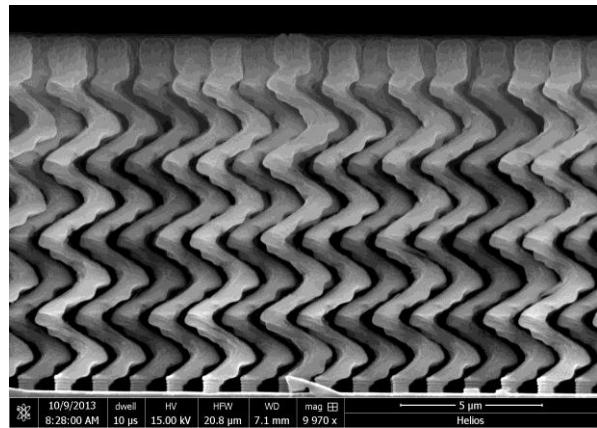
The Si nanospring films were grown at a rate of 10 Å/s and an incident angle of 85°, with a substrate rotation rate of 4.2°/min for 4-turn springs and 10.6°/min for 10-turn springs. The 4-turn springs were approximately open-coiled, whereas the 10-turn were close-coiled (screw-like), as shown in Figures 2(a-d). The degree of spring intertwining varied with seed spacing, with larger spacing and smaller spring pitch resulting in less overlap between springs, Figures 3(a-d). The wire comprising the open-coiled springs had elliptical cross-section and the major and minor axes of the wire were measured from Scanning Electron Microscopy (SEM) images. The measured geometrical parameters of the Si springs are listed in Table 1. Half of the spring films were capped with an additional 1000-nm layer of solid Si to facilitate shear testing. The capping layer was deposited at 10 Å/s and a substrate rotation rate of 2400°/min, with an incident angle of 20°. The capping layer was continuous in the case of 4-turn springs that demonstrated significant overlap, Figure 3(a,b), while the capping layer was not as cohesive in the case of 10-turn springs, especially those with 1500 nm seed spacing due to the large spacing between individual springs, Figure 3(d).

Table 1. Geometrical parameters of the Si spring films fabricated for this study.

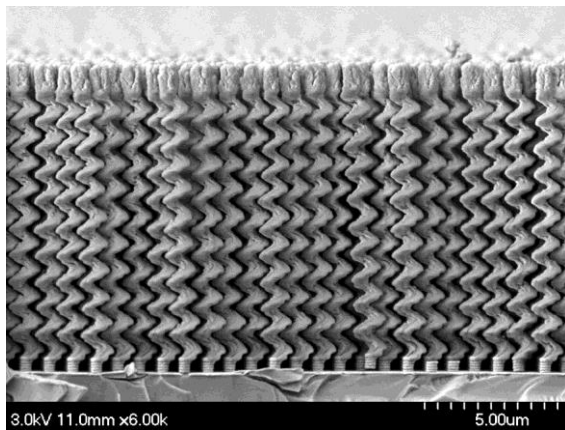
Spring Type (number of turns, seed spacing)	Coil diameter (nm)	Major axis of the wire (nm)	Minor axis of the wire (nm)	Pitch (nm)
4 turns, 900 nm	1530	760	430±50	2500
4 turns, 1500 nm	1570	940	565±60	2500
10 turns, 900 nm	1060	700	400±30	1000
10 turns, 1500 nm	1320	870	610±30	1000



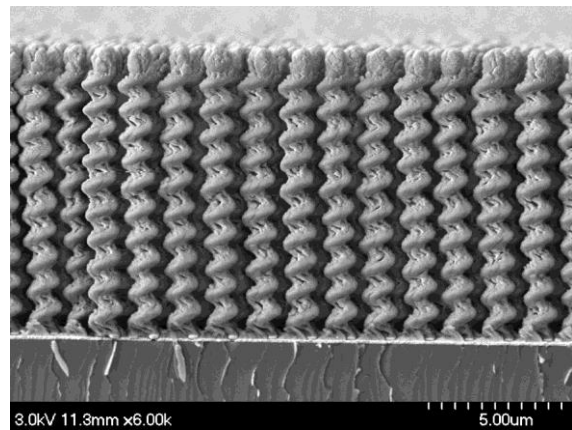
(a)



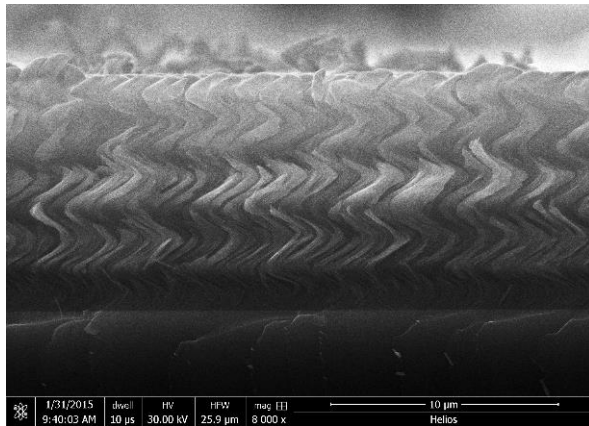
(b)



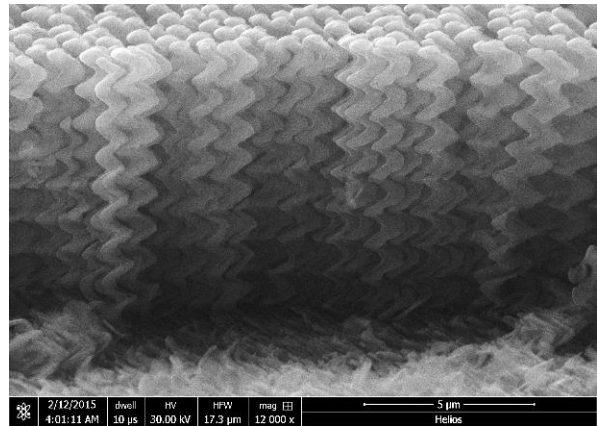
(c)



(d)



(e)



(f)

Figure 2. Side views of Si spring films comprised of (a) 4-turn coils with 900 nm seed spacing, (b) 4-turn coils with 1500 nm seed spacing, (c) 10-turn coils with 900 nm seed spacing, (d) 10-turn coils with 1500 nm seed spacing, (e) 4-turn coils on unseeded substrate, and (f) 10-turn coils on unseeded substrate.

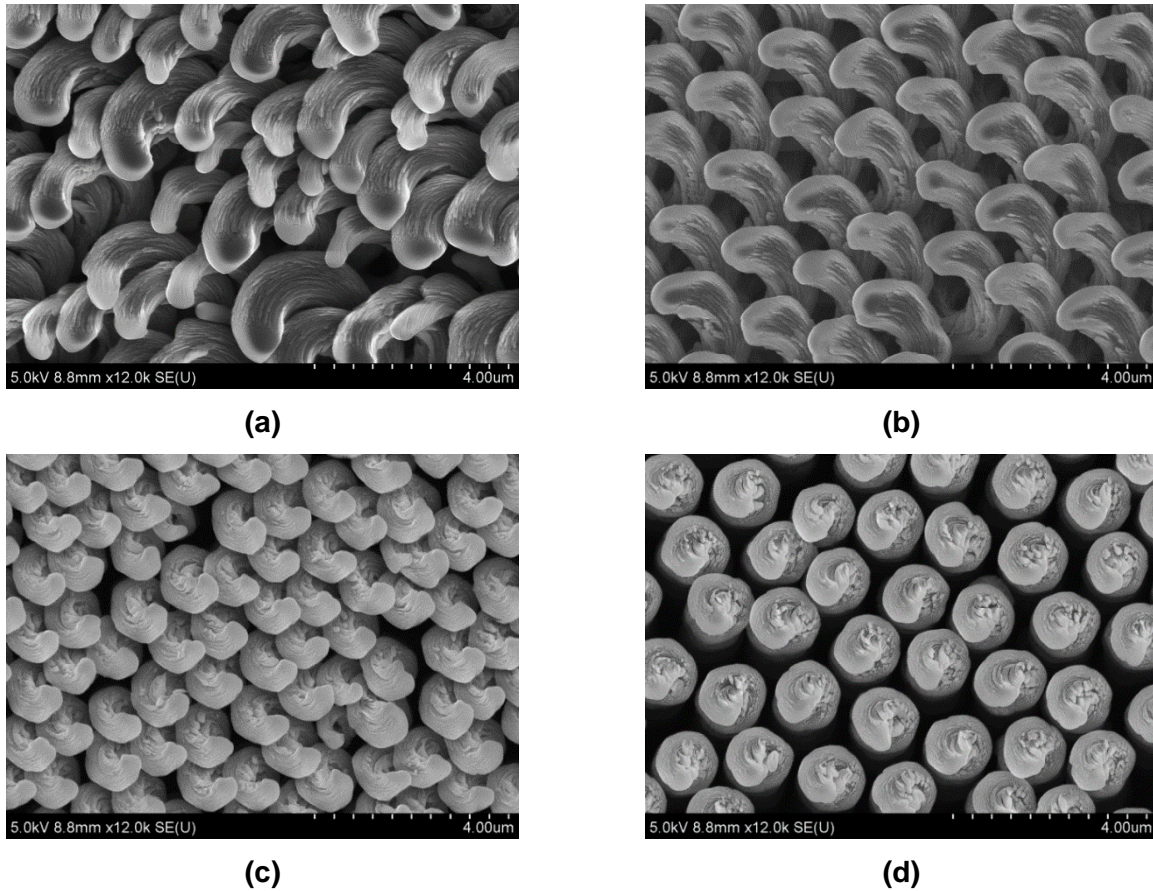


Figure 3. Top views of Si spring films comprised of (a) 4-turn coils with 900 nm seed spacing, (b) 4-turn coils with 1500 nm seed spacing, (c) 10-turn coils with 900 nm seed spacing, and (d) 10-turn coils with 1500 nm seed spacing.

II.2 Fabrication of Cu Spring Films

The Cu spring films were also fabricated at Micralyne using GLAD on seeded silicon wafers. 10- μm high, 10-turn Cu spring films, Figure 4(a-d), were deposited with four different seed spacings: 2000 nm, 2400 nm, 2800 nm, and 3200 nm. Portions of the wafer also contained unseeded Cu springs, Figure 4(e). Larger seed spacing resulted in larger coil diameter and less overlap between adjacent springs. Thus, the interaction between adjacent springs decreases as the seed spacing increases. The Cu films were deposited at the rate of 20 $\text{\AA}/\text{s}$, incident angle of 86° , and substrate rotation speed of $7.1^\circ/\text{min}$. The geometry of 10-turn Cu springs was quite different from that of 10-turn Si springs, due to the different deposition rates and substrate rotation speeds: the deposition rate of 10-turn Si films was 10 $\text{\AA}/\text{s}$ and the rotation rate was $10.6^\circ/\text{min}$, while the deposition rate of 10-turn Cu films was 20 $\text{\AA}/\text{s}$ and the rotation rate of $7.1^\circ/\text{min}$. These values correspond to a deposition rate of 56.6 \AA per degree of rotation for Si

and 169 Å per degree of rotation for Cu, thus Cu the springs were much larger (microsprings) than the Si springs (nanosprings).

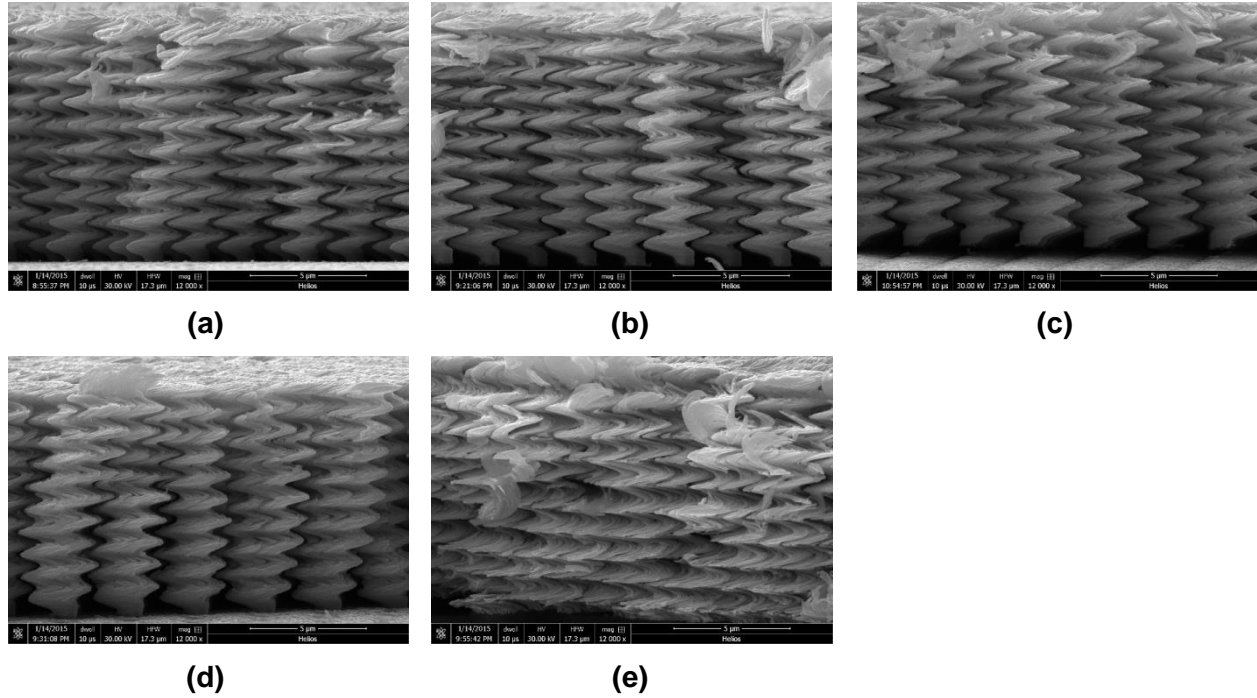


Figure 4. Cu spring films comprised of 10-turn coils and **(a)** 2000 nm, **(b)** 2400 nm, **(c)** 2800 nm, **(d)** 3200 nm seed spacing, and **(e)** deposited on unseeded substrate.

II.3 Film Compression Experiments

Compression tests were performed on uncapped seeded and unseeded Si and Cu spring films. Precise circular test areas of ~100 µm diameter were prepared using a Focused Ion Beam (FIB). First, a ring with an outer diameter of 130 µm and inner diameter of 100 µm was milled, as shown in Figure 5(a). The springs outside of each cylindrical area were then removed, leaving behind test specimens such as the one shown in Figure 5(b). As a result of the initial milling, a fused layer of Si formed on the outer surface of the test specimen, which was removed by low power FIB ion-milling, to produce the final circular test area, shown in Figure 5(c).

Compression tests were performed with a commercial Hysitron TI 950 TriboIndenter and a 188-µm diameter circular flat punch made of sapphire, while the methodology for instrumented nanoindentation [30-34] was followed to analyze the experimental force-displacement data. Each test area was subjected to 10 loading-unloading cycles between 0 MPa and a maximum of 0.5, 5, 10, 15, 20, 25, 30, 40, or 50 MPa. Each specimen was subjected to additional 10-cycles of loading and unloading in a ±10% range about each maximum stress value. The compressive stiffness, E , was calculated from the slope of the force vs. displacement plots as:

$$E = k_T \frac{h}{A} \quad (1)$$

where k_T is the slope of the curve constructed with data in the $\pm 10\%$ range of each peak stress value, h is the mean height of the spring film where k_T was computed, and A is the test area. A sample plot of the load vs. displacement for a 4-turn, 900 nm seeded Si spring film loaded to 5 MPa peak stress is shown in Figure 6. Because of the large area of indentation, recalibration of the commercial indenter was required to account for the test system compliance: compression tests were performed on clean substrate to measure the system (substrate, cylindrical punch, adhesive and indenter) stiffness. Then, the true stiffness of the spring film, k , was computed as:

$$k = \frac{k_T k_S}{k_T - k_S} \quad (2)$$

where k_T is the total measured stiffness and k_S is the stiffness of the system.

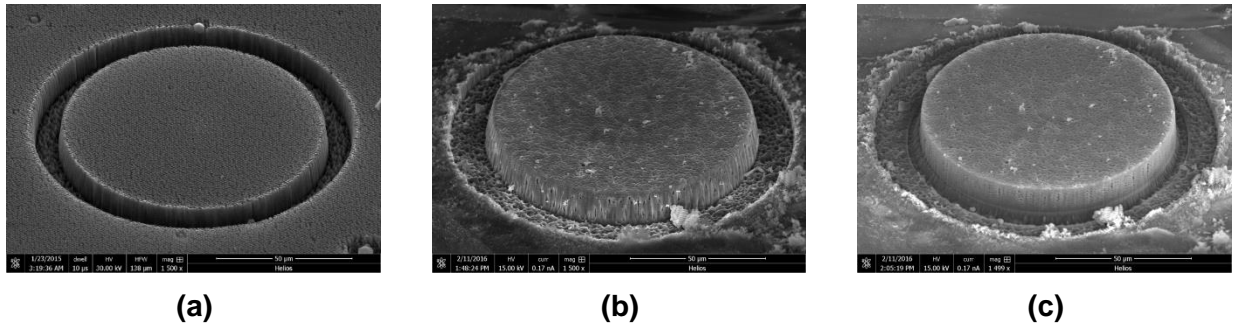


Figure 5. Test area definition for a film with 10-turn unseeded springs: **(a)** Initial FIB milling of a cylindrical specimen, **(b)** springs removed outside the cylinder, **(c)** fine FIB ion-milling removed the fused springs at the edges of the test area.

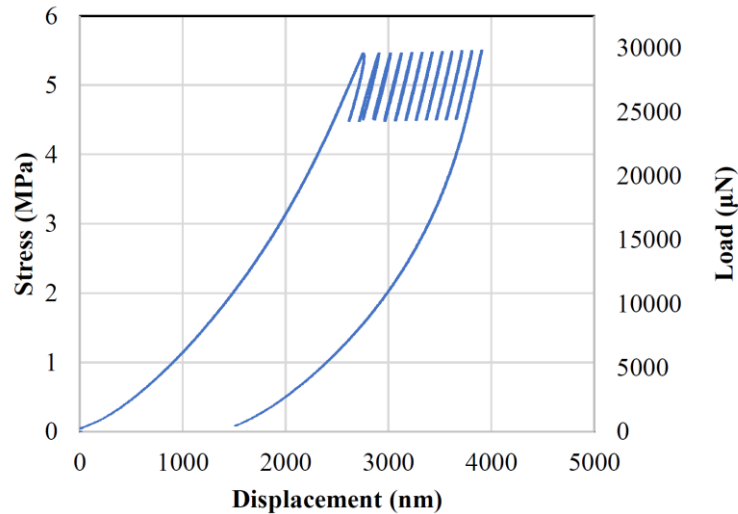


Figure 6. Load vs. displacement curve of a Si film comprised of 4-turn springs deposited with 900 nm seed spacing and subjected to cyclic loading in the range 0-5 MPa. For clarity, each loading-unloading cycle with amplitude of 10% of the mean has been separated in the plot.

II.4 Film-level Shear Experiments

Shear tests were performed on capped films by using a home-built apparatus [35-37]. The force was measured with a 50 g load cell and in-plane shear displacements were imposed via a linear PZT actuator. The test areas were FIB-milled and had rectangular dimensions of $100 \times 200 \mu\text{m}^2$. Following a procedure similar to that outlined in Figure 5, perfectly rectangular test areas were created, as shown in Figures 7(a,b). For shear testing, the test apparatus was placed under an optical microscope equated with a CCD camera to record images of the sample surface at 5 fps. In-plane displacements were then computed from the optical images using Digital Image Correlation (DIC), to determine the net displacement of the test area, which, in turn, was used to construct the shear force vs. displacement curve, similar to the example shown in Figure 8.

The slope of the shear force vs. displacement plot, k_{shear} , was used to calculate the shear modulus of the film, G_{shear} using the equation:

$$G_{shear} = k_{shear} \frac{H}{A} \quad (3)$$

where H is the height of the spring film not including the cap and A is the test area. A sample plot is shown in Figure 8.

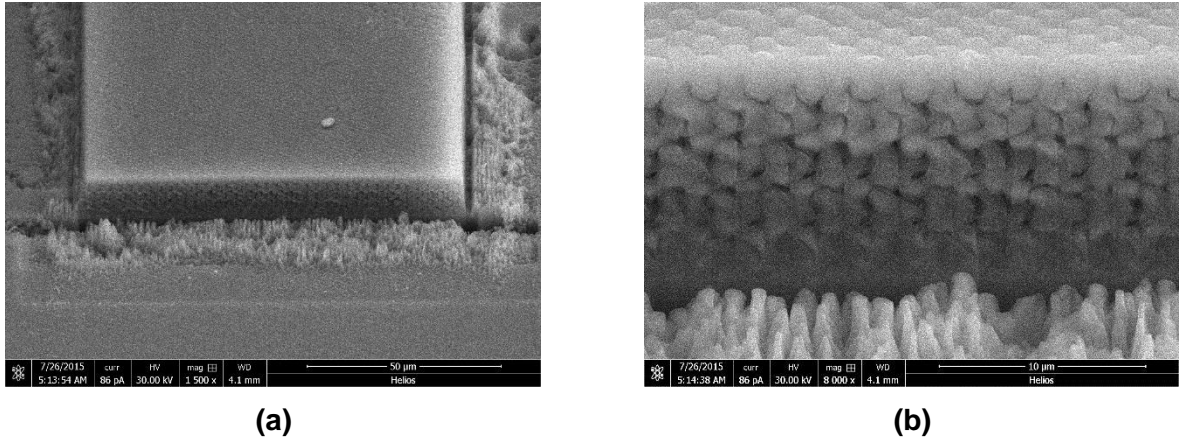


Figure 7. Test area in a film comprised of 4-turn Si springs with 1500 nm seed spacing after ion-milling, shown at (a) 1,500 \times , and (b) 8,000 \times magnification.

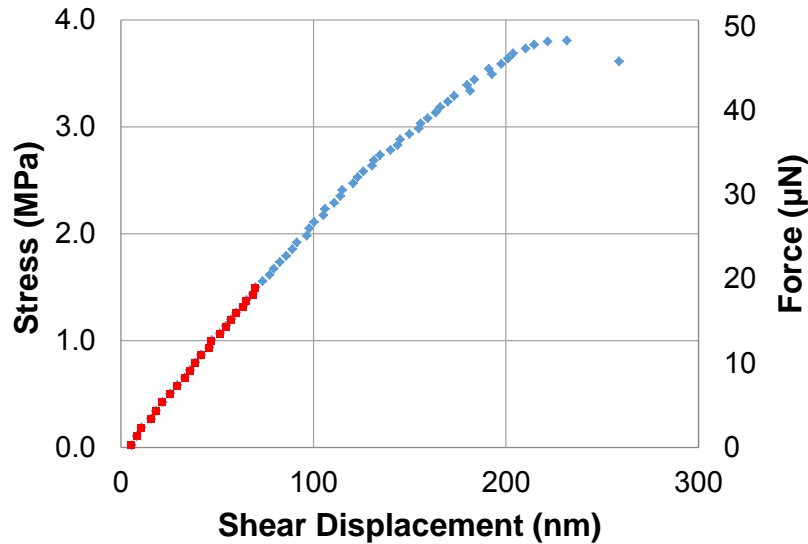


Figure 8. Shear stress vs. displacement plot of a Si film comprised of 10-turn springs with 2000 nm seed spacing. The red data points were used to compute the initial film shear stiffness.

II.5 Mechanical Tests of Individual Si Springs

The tension/compression and bending behavior of individual springs were quantified with the aid of MEMS devices using a method developed before by this group [35]. The stiffness of the compression/tension and shear MEMS devices was measured by loading them against devices of known stiffness [38]. A side and top view of an isolated 4 turn, 900nm seeded Si spring is shown in Figure 9(a,b). The mounted springs were fixed onto the MEMS devices via platinum (Pt) tabs that were deposited with a FIB. Images before and after deposition of the Pt tabs showed no or minimum Pt deposition on the test specimens. The Pt tabs were fully constrained the ends of the springs, thus creating approximate fixed-fixed boundary conditions. Figures 10(a-d) show the four different types of Si springs mounted before compressive testing, whereas Figures 11(a-d) show the same types of Si springs mounted for shear testing. The first two test structures in Figures 10(a-d) and Figures 11(a-d) are spring-like, the third has a spring-like structure with much smaller coil diameter, whereas the fourth is closer to a staircase shape.

The mechanical response of the individual Si springs was investigated for springs retrieved only from seeded areas; the density of springs in unseeded areas was too high, thus making the removal of intact unseeded springs impractical. The springs were subjected to tension or compression at a loading rate of 30 nm/sec. Testing was performed under an optical microscope and images were captured at a 400× magnification. At least three specimens of each spring type were tested.

The initial tensile/compressive stiffness of the springs was measured from the slope of the linear segment of the load vs. spring extension/compression curves. The applied load was calculated from changes in the opening of the loadcell, namely the motion of areas “2” and “3” in Figure 12. The spring extension/compression was obtained from the crosshead displacement

which corresponds to the relative motion of areas “1” and “2” in Figure 12. A comparison of the relative motion of the two areas marked as “1” provided a measure for any unintentional bending load. The motion of the two areas marked as “1” was found to be virtually identical.

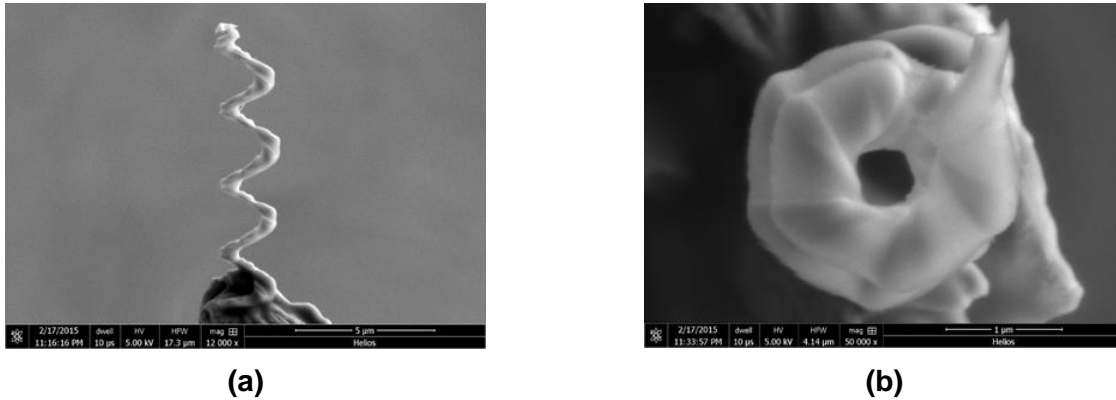


Figure 9. (a) Side and (b) top view of a Si spring with 4 turns.

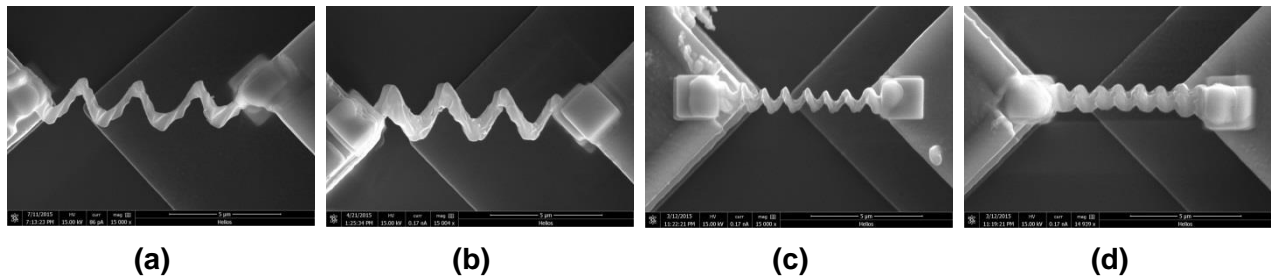


Figure 10. Si springs mounted on MEMS devices for uniaxial compression testing isolated from films with (a) 4-turn coils with 900 nm seed spacing, (b) 4-turn coils with 1500 nm seed spacing, (c) 10-turn coils with 900 nm seed spacing, and (d) 10-turn coils with 1500 nm seed spacing.

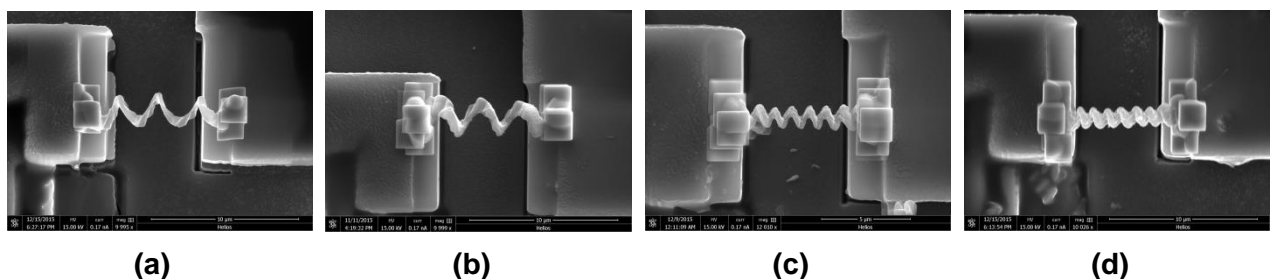


Figure 11. Si springs mounted on MEMS devices for shear testing, isolated from films with (a) 4-turn coils with 900 nm seed spacing, (b) 4-turn coils with 1500 nm seed spacing, (c) 10-turn coils with 900 nm seed spacing, and (d) 10-turn coils with 1500 nm seed spacing.

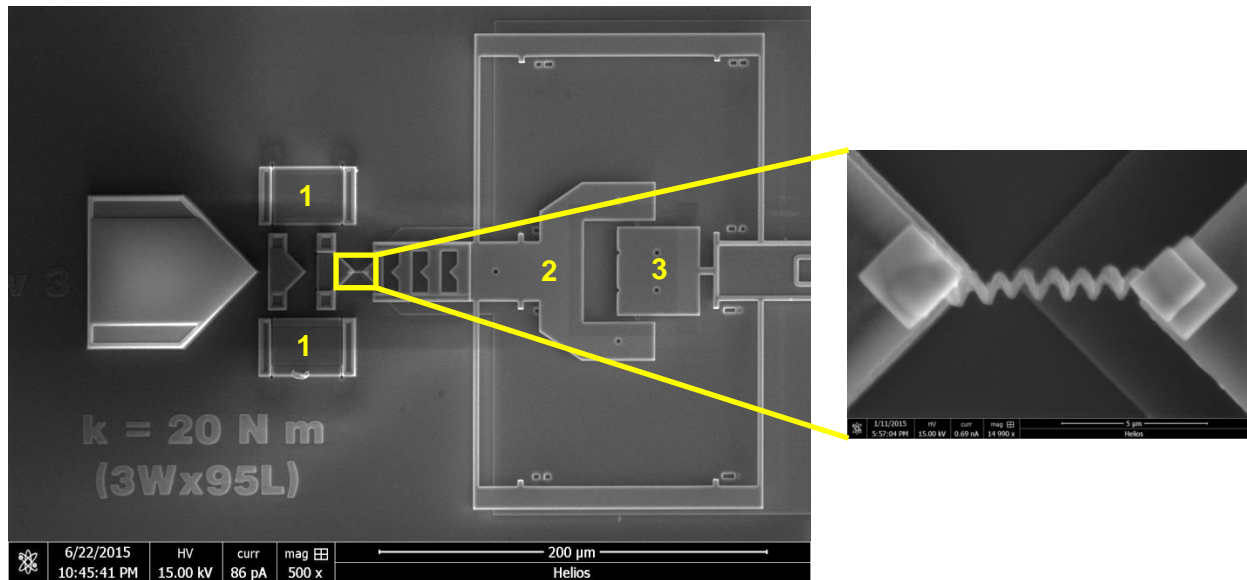


Figure 12. A 10-turn spring mounted on a tension/compression MEMS device. DIC was performed to compute the displacements of areas “1”, “2”, “3” in the left figure.

Similarly, the bending stiffness of individual springs was measured from the slope of the linear segment of the load vs. lateral deflection curves. The bending force was calculated from the relative motion of areas “2” and “3” in Figure 13. The lateral deflection of the spring was computed from the change in distance between areas “1” and “2” in Figure 13. Both the loadcell opening and the lateral spring deflection were computed via DIC which was performed on dark-field optical microscopy images obtained at 400× magnification, resulting in an accuracy of 0.1 pixels (20-25 nm). Finally, the effect of the lateral interactions between springs at the film level was investigated by mounting bundles of two or more springs onto the MEMS devices. Figures 14(a,b) show two 10-turn Si springs mounted for mechanical testing on a tension/compression and on a bending MEMS device, respectively.

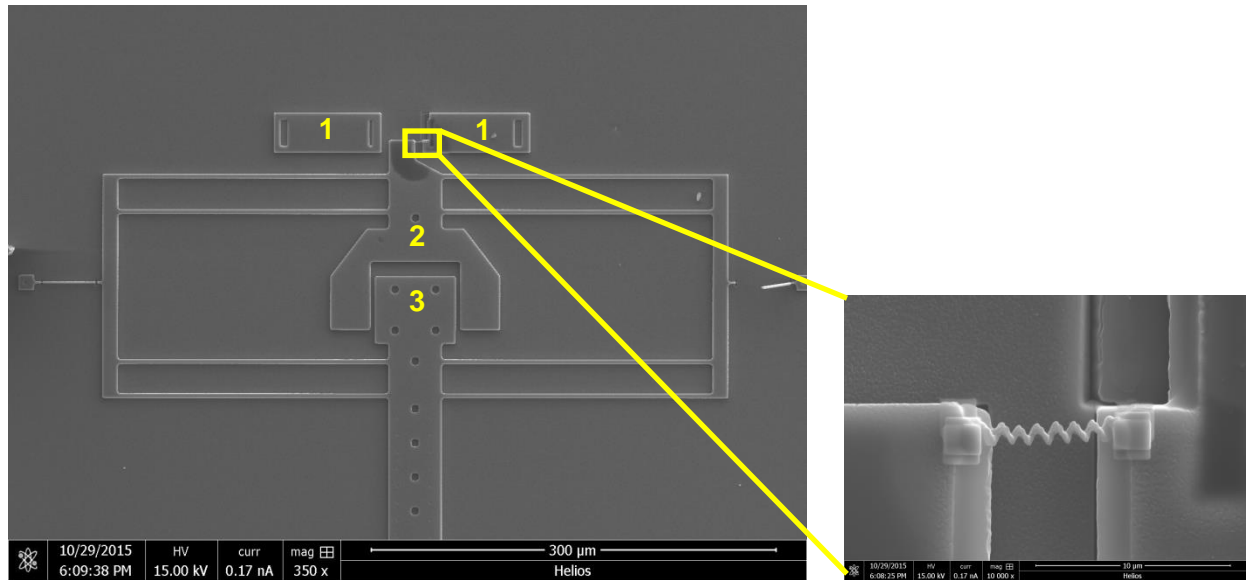
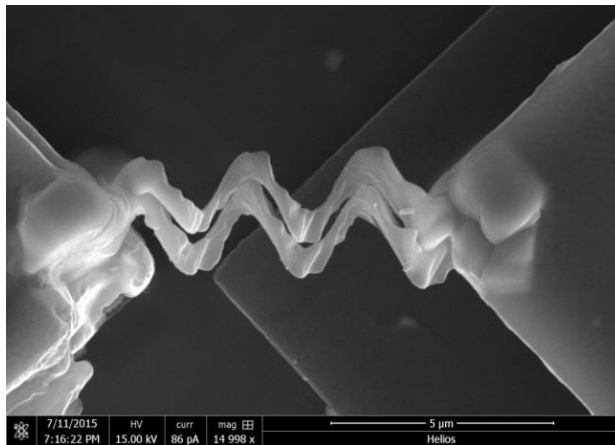
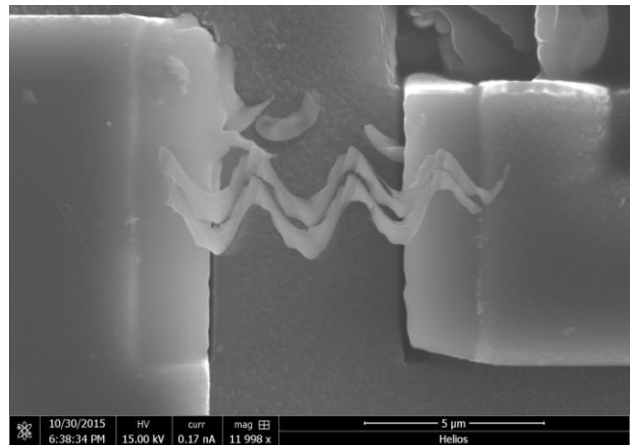


Figure 13. A 10-turn spring mounted onto a MEMS device for shear testing. DIC was performed to compute the displacements of areas “1”, “2”, “3” in the figure.



(a)



(b)

Figure 14. Two 4-turn springs directly transferred and mounted on MEMS devices for **(a)** compression and **(b)** bending testing.

II.6 Analytical Models for Helical Springs

In order to assess whether the mechanical behavior of the individual springs tested in this research program approximates that of an ideal coil, the experimentally determined tensile/compressive stiffness values were compared to predictions by analytical models for spring extension/compression and bending. Wahl derived equations for springs under uniaxial loading and for different types of boundary conditions [39,40]. For a spring with both ends fixed, the axial stiffness is can be estimated from:

$$k_a = \frac{Gd^4}{8D^3N} (\psi'_1)^{-1} \quad (4)$$

where G is the shear modulus, d is the wire diameter of the spring, D is the coil diameter, N is the number of turns of the spring and ψ'_1 is a correction factor that takes into account the boundary conditions and is defined as:

$$\psi'_1 = \frac{\sin \alpha - \sin \alpha_0}{\cos^3 \alpha_0 \left[\sin \alpha - \sin \alpha_0 + \frac{EI}{GI_p} \tan \alpha (\cos \alpha_0 - \cos \alpha) \right]} \quad (5)$$

where α is the pitch angle at a given displacement, α_0 is the initial pitch angle, E is the elastic modulus, I is the moment of inertia and I_p is the polar moment of inertia. The pitch angle is given by:

$$\tan \alpha = \frac{h_p}{\pi(D + d)} \quad (6)$$

where h_p is the pitch length of the spring.

Ancker and Goodier [41,42] derived the following equation for the axial stiffness of a spring in tension, assuming radial symmetry (every cross-section of the spring experiences the same load):

$$k_a = \frac{Gd^4}{8D^3N} \left[1 - \frac{3d^2}{16D^2} + \frac{1 - \nu}{2(1 + \nu)} \tan^2(\alpha) \right]^{-1} \quad (7)$$

Analytical models can provide approximate solutions for a limited spectrum of boundary conditions. Zhang and Zhao [43] investigated the effect of boundary conditions on the mechanical response of springs with round and square coils via a Finite Element Analysis (FEA). Springs with fixed ends had 2-3 times higher effective stiffness when compared to springs with one free end, which shows the significant role of boundary conditions.

Timoshenko derived an equation for the lateral stiffness of a spring by taking into account the deflection due to the bending moment and the shearing force [44]. The transverse stiffness in this case is given by:

$$k_t = \frac{6EI}{\pi N h^2 D} \left[\frac{1 + \sin^2(\alpha)}{\cos(\alpha)} + \frac{3D^2}{4h_p} + \frac{EI}{GI_p} \cos(\alpha) \right]^{-1} \quad (8)$$

In the case that the spring index (=coil diameter/wire diameter) is not large, the torsional rigidity represented by the term Gl_p is multiplied by the correction factor β :

$$\beta = 1 + \frac{3 \left(\frac{d}{D}\right)^2}{16 \left[1 - \left(\frac{d}{D}\right)^2\right]} \quad (9)$$

Finally, Lee et al. [45] derived the lateral stiffness equation for a spring with one end free and the other fixed against rotation:

$$\begin{aligned} k_t = & \left[\frac{\omega l}{GA} \theta + \left(\frac{1}{EA} - \frac{\alpha}{GA} \right) \frac{R^2}{l} \left(\frac{\theta}{2} - \frac{\sin 2\theta}{4} \right) \right. \\ & + \frac{l}{EI} \left[\left(1 - \frac{p^2}{4\pi^2 l^2} \right) \frac{R^2}{2} \theta - \frac{R^2}{4} \sin 2\theta + \left(1 - \frac{R^2}{2l^2} \right) \frac{2\pi}{3p} h_p^3 \right] + \frac{1}{GJ} \left[\frac{p^2 R^2}{8\pi^2 l} \theta \right. \\ & + \left. \left. \frac{\pi R^2 h_p^3}{3pl} \right] \right. \\ & + \left(\frac{1}{GJ} \right. \\ & - \frac{1}{EI} \left[\left(\frac{h_p^2 R^2}{4l} - \frac{5p^2 R^2}{32\pi^2 l} \right) \sin 2\theta + \frac{p R^2 h_p}{8\pi l} (3 - 3 \cos 2\theta - 2\theta \sin 2\theta) \right. \\ & + \left. \left. \left. \frac{p^2 R^2}{16\pi^2 l} (3\theta \cos 2\theta + \theta^2 \sin 2\theta) \right] \right]^{-1} \right] \quad (10) \end{aligned}$$

where ω is a shear correction factor and θ is the total angle of rotation and equal to $2\pi n$.

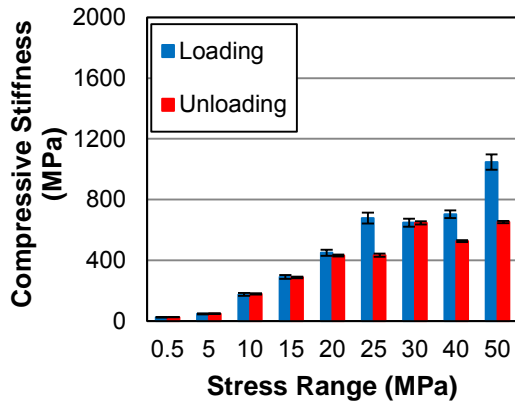
These analytical expressions are utilized to obtain estimates for comparison with the experimental results discussed in the next sections of this report.

III. RESULTS AND DISCUSSION

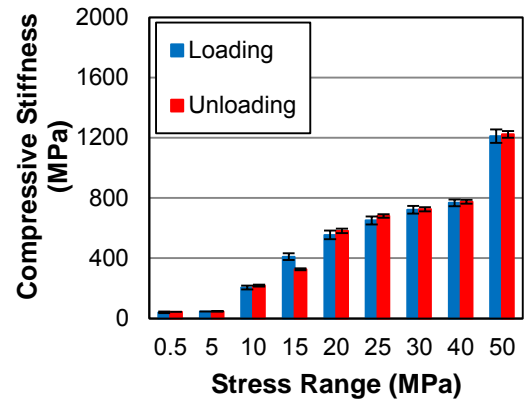
III.1 Compressive Behavior of Si Films

The compressive moduli of Si spring films, as determined using Equations (1) and (2) are shown in Figures 15(a-f) for uncapped Si films and in Figures 16(a-f) for capped Si films. In the majority of uncapped films, the effective compressive modulus increased with applied stress, potentially due to contact between adjacent springs. In most cases, the loading moduli of uncapped and capped seeded springs were larger than the unloading moduli of the same springs, especially at high applied stresses, potentially signifying damage in the form of spring buckling or tilting occurring during loading at high stresses which resulted in reduced stiffness. Specifically, the 4-turn, 900 nm, 10-turn, 900 nm and 10-turn, 1500 nm springs films demonstrated loading moduli that were greater by 60%, 11%, and 29%, respectively, with reference the unloading value, than the unloading moduli at the highest applied stress of 50 MPa. The unseeded spring films exhibited smaller variations between loading and unloading moduli, which did not exceed 13%. Notably, 10-turn, 1500 nm seeded capped films exhibited a decrease in the effective compressive modulus at high stresses and large difference between the loading and unloading moduli at 30 and 40 MPa (by 115%), which may be the result of fracture of the capping layer; as shown in Figure 3(d), the particular films had no overlap between springs and therefore the cap was easier to fracture. On the other hand, the capping layer restricted spring end rotations and independent bending and tilting, thus leading to higher effective compressive moduli compared to uncapped films whose top end was unconstrained. Furthermore, the deviation between the loading and unloading moduli of capped films was smaller than for uncapped films because the capping layer did not allow for independent spring tilting during loading, and thus less damage that would reduce the unloading film stiffness.

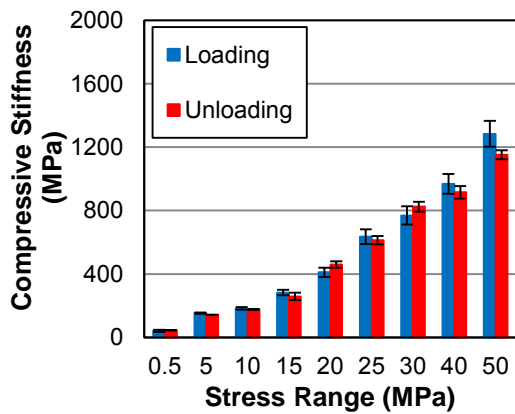
A direct comparison between the average unloading moduli of the 4-turn and 10-turn uncapped and capped Si spring films is provided in Figures 17(a,b) and Figures 18(a,b) in logarithmic axes for better definition of the data at low stresses. In most cases the unloading modulus of capped films was larger than the uncapped counterparts, with the exception of films comprised of 10-turn coils with 900 nm seed spacing and unseeded Si films with 10-turn coils mainly at high stresses. At the lowest stress of 0.5 MPa, which is also the most technologically relevant, the stiffness of uncapped films with 4-turn springs was 33.9 ± 1.0 MPa for 900 nm seed spacing, 26.3 ± 0.4 MPa for 1500 nm seed spacing, and 43.8 ± 0.9 MPa for unseeded springs. In comparison, the stiffness of capped films with 4-turn springs was 20.7 ± 0.3 MPa for 900 nm seed spacing, 12.9 ± 0.7 MPa for 1500 nm seed spacing, and 38.3 ± 0.8 MPa for unseeded springs. In the case of films comprised of 10-turn coils, the stiffness of uncapped films was 32.8 ± 1.6 MPa for 900 nm seeding, 45.2 ± 1.4 MPa for 1500 nm seeding, and 96.1 ± 5.5 MPa for unseeded films, whereas for the capped films, 38.6 ± 1.3 MPa for 900 nm seed spacing, 94.5 ± 5.5 MPa for 1500 nm seed spacing, and 21.8 ± 0.9 MPa for unseeded films. For a tenfold increase in stress to 5 MPa, the stiffness of uncapped films with 4-turn springs was 48.6 ± 1.1 MPa for 900 nm spacing and 46.9 ± 0.4 MPa for 1500 nm seed spacing, while unseeded spring films had the highest stiffness of 59.9 ± 1.3 MPa. For the same stress, capped films had comparable stiffness. The 10-turn uncapped spring films demonstrated a different trend, with increasing stiffness from 91.1 ± 1.9 MPa for unseeded spring films, to 142.5 ± 1.5 MPa for films with 900 nm seed spacing, and finally 216.4 ± 4.3 MPa for 1500 nm seeding. Similar trends were observed for the capped 10-turn films, with unseeded film stiffness of 100.9 ± 2.5 MPa, 132.2 ± 1.6 MPa for 900 nm seed spacing, while springs with 1500 nm seed spacing demonstrated a fourfold increase, compared to 0.5 MPa stress, to 420.13 ± 4.3 MPa.



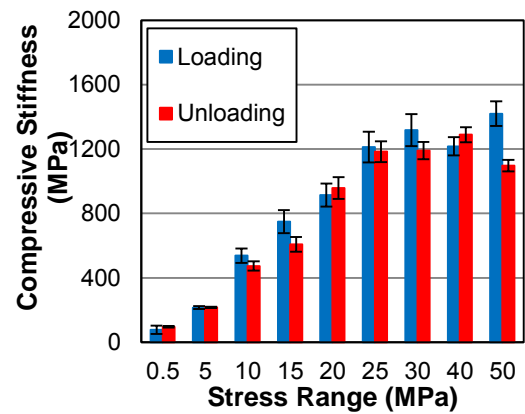
(a)



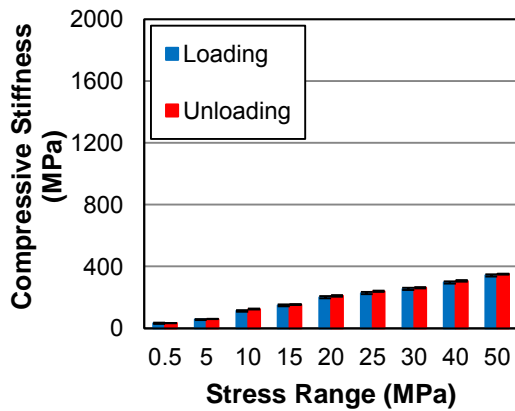
(b)



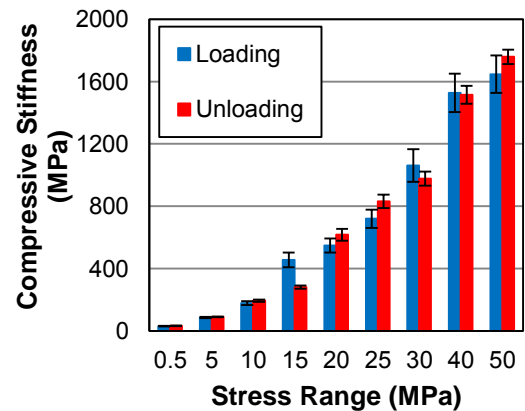
(c)



(d)



(e)



(f)

Figure 15. Compressive stiffness (modulus) of uncapped films comprised of (a) 4-turn springs with 900 nm seed spacing, (b) 4-turn springs with 1500 nm seed spacing, (c) 10-turn springs with 900 nm seed spacing, (d) 10-turn springs with 1500 nm seed spacing, (e) 4-turn springs on unseeded substrate, and (f) 10-turn springs on unseeded substrate.

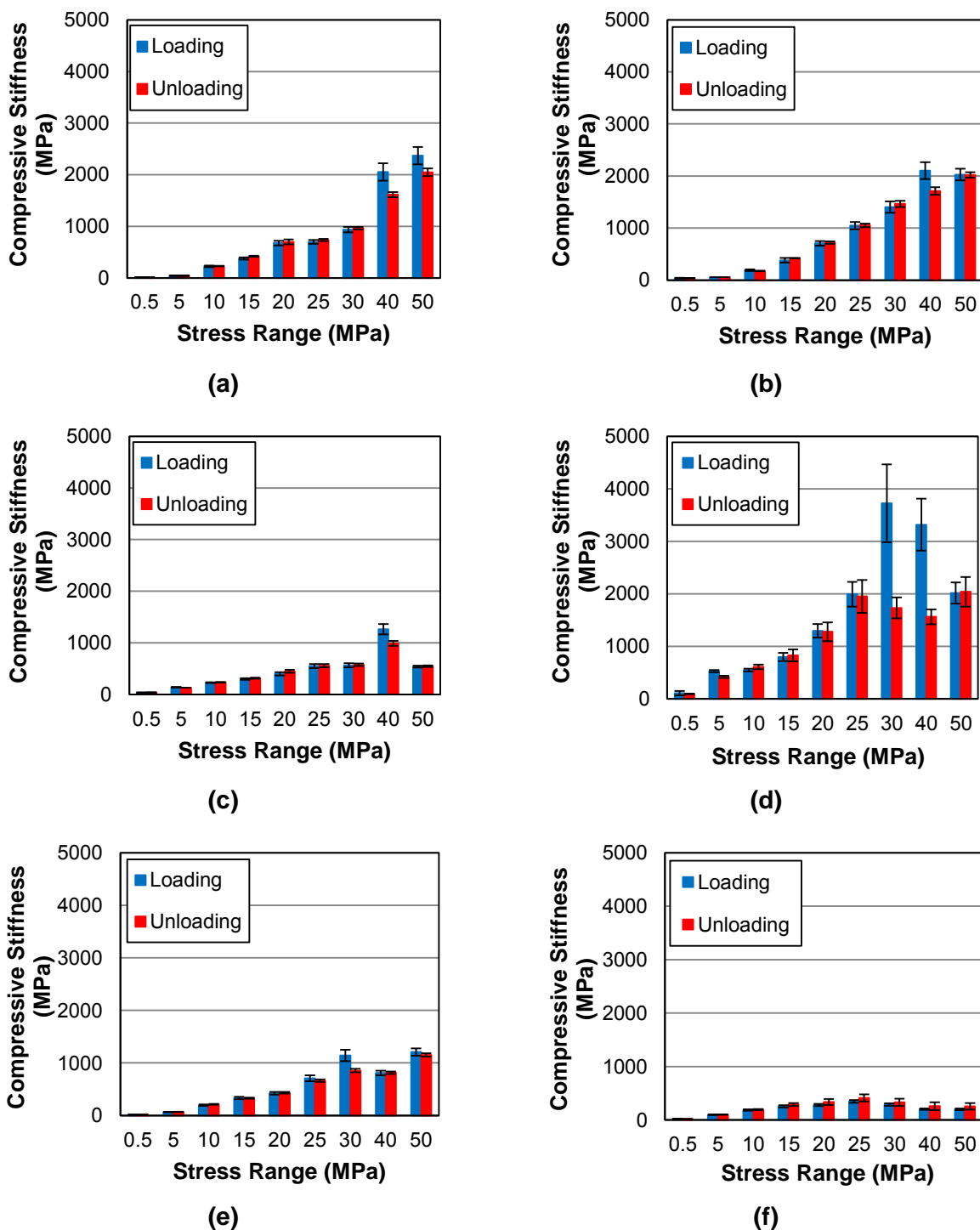
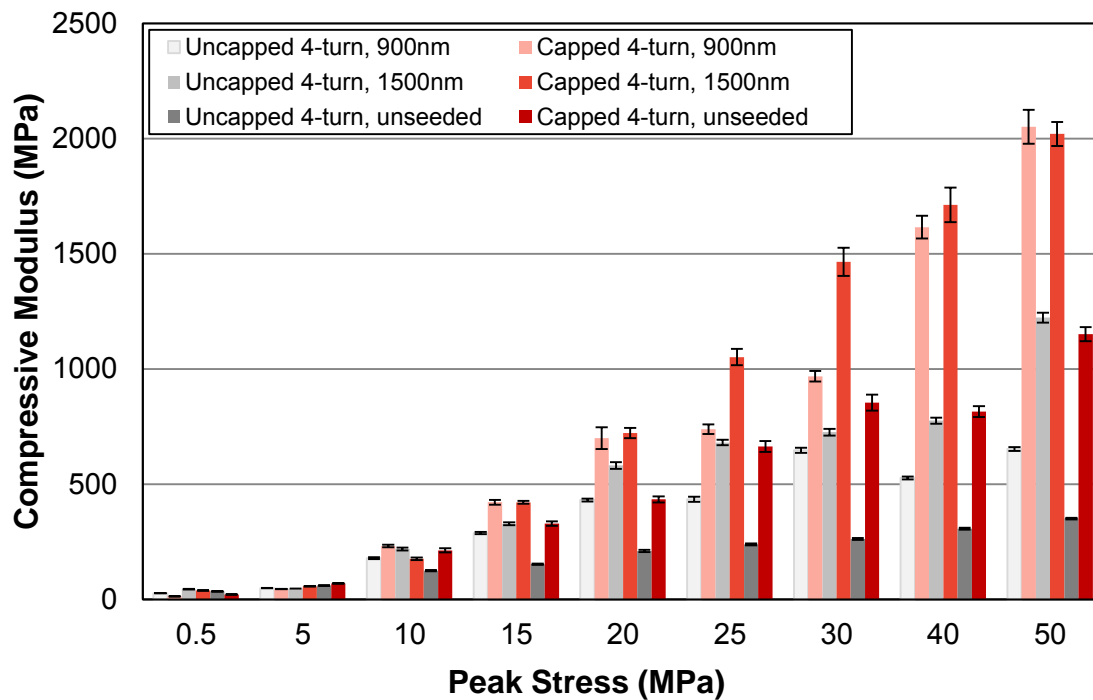
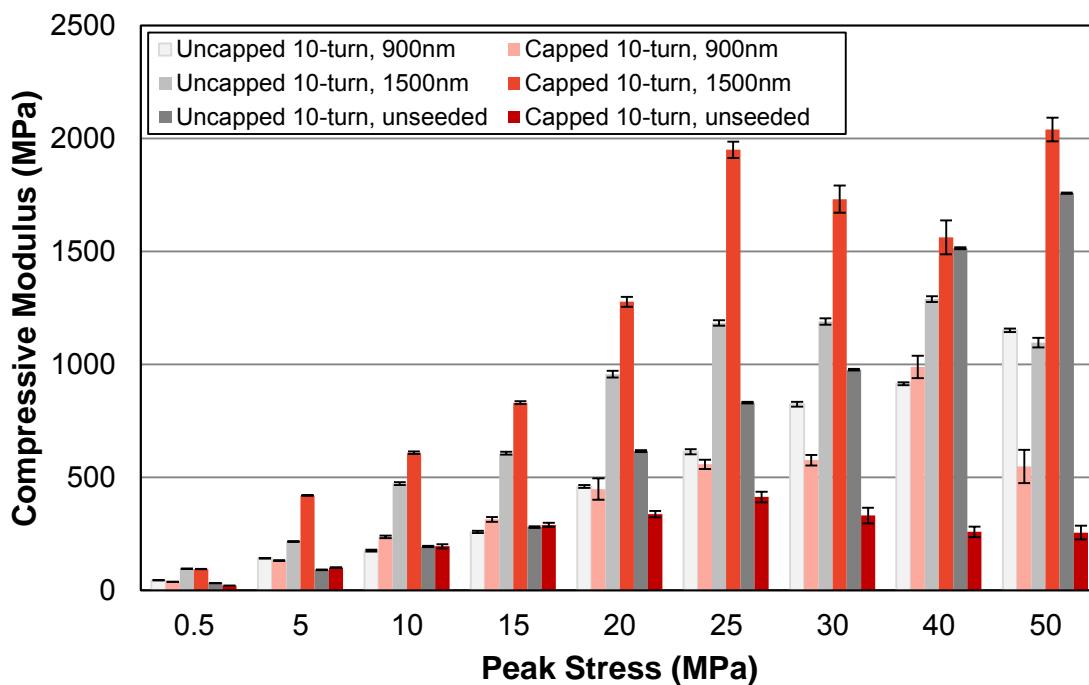


Figure 16. Compressive stiffness (modulus) of capped films comprised of (a) 4-turn springs with 900 nm seed spacing, (b) 4-turn springs with 1500 nm seed spacing, (c) 10-turn springs with 900 nm seed spacing, (d) 10-turn springs with 1500 nm seed spacing, (e) 4-turn springs on unseeded substrate, and (f) 10-turn springs on unseeded substrate.

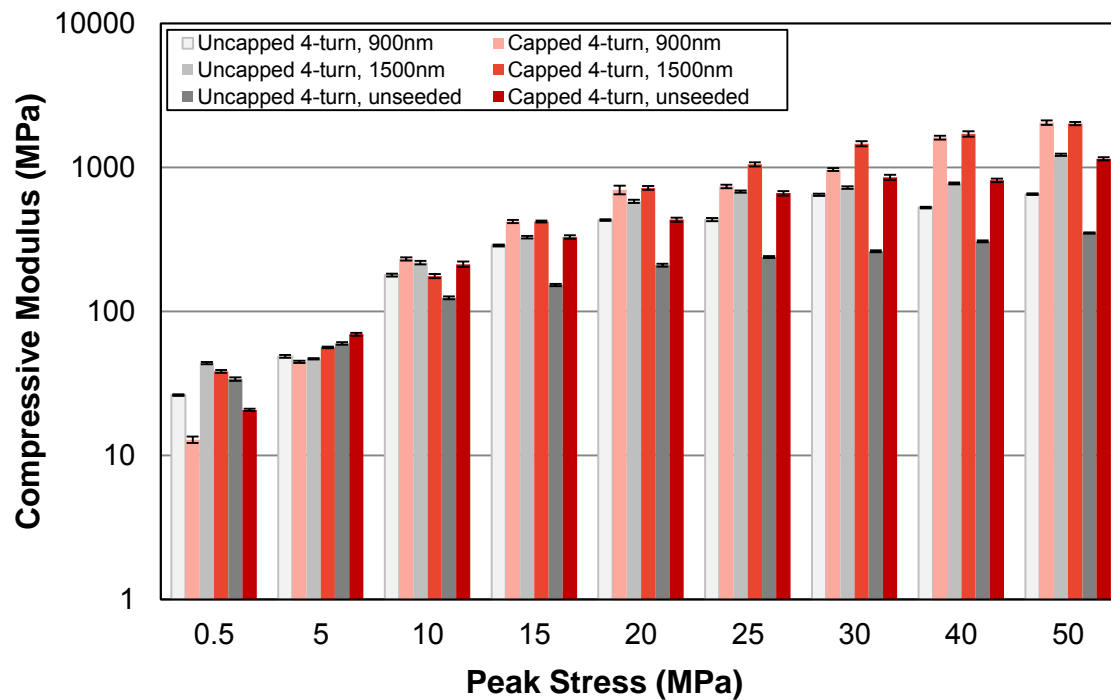


(a)

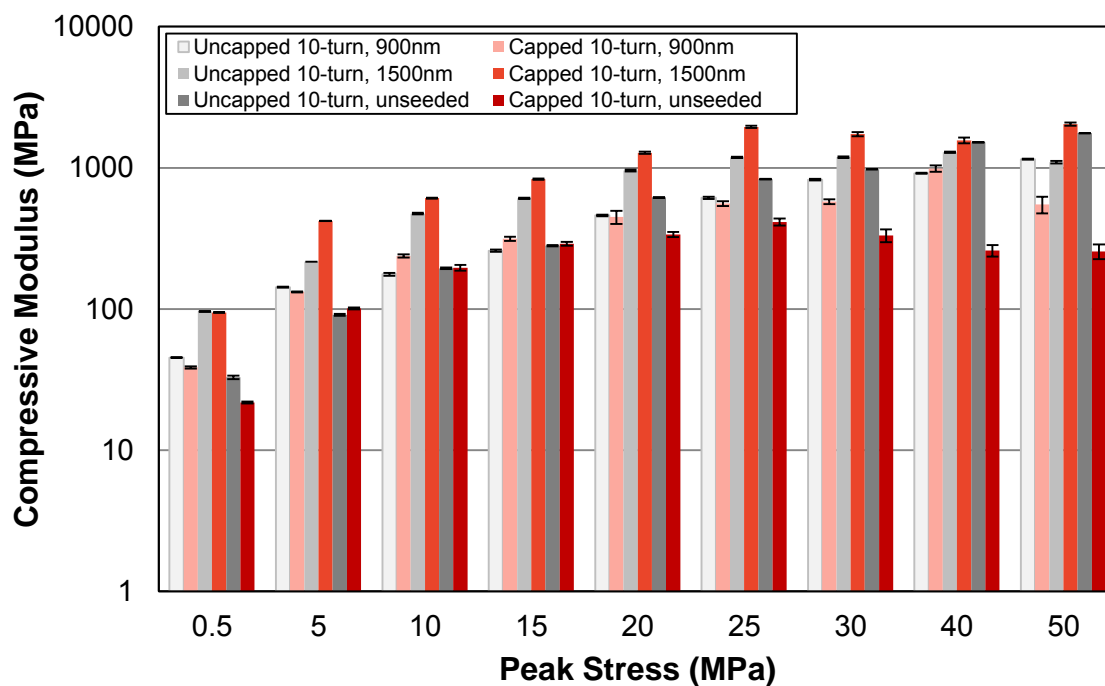


(b)

Figure 17. Compressive unloading modulus of uncapped and capped films with (a) 4-turn, and (b) 10-turn Si springs, subjected to different peak stresses.



(a)



(b)

Figure 18. Compressive unloading modulus of uncapped and capped films with (a) 4-turn, and (b) 10-turn Si springs, subjected to different peak stresses. The data are the same as in Figure 17, here presented in logarithmic scale for better definition of the modulus values at low stresses.

At the other extreme, at the highest applied stress of 50 MPa, uncapped films with 4-turn springs experienced a large variation in stiffness, starting at 350 ± 3 MPa for unseeded springs, to 528 ± 3 MPa for springs with 900 nm seed spacing, and 1223 ± 22 MPa for 1500 nm seed spacing. The stiffness of the corresponding capped films was 1151 ± 31 MPa for unseeded springs, 868 ± 5 MPa for films with 900 nm seed spacing, and 2021 ± 52 MPa for 1500 nm seed spacing, namely all corresponding values were higher for capped films. A reverse trend was recorded for uncapped films with 10-turn coils subjected to 50 MPa: the stiffness for 900 nm seed spacing was 1758 ± 46 MPa, 1152 ± 29 MPa for 1500 nm seeding, and 1097 ± 35 MPa unseeded springs. In comparison to uncapped 10-turn spring films, capped films with 900 nm seed spacing had a stiffness of 549 ± 16 MPa, 2040 ± 283 MPa for 1500 nm seed spacing, and 256 ± 60 MPa for unseeded films, namely a monotonic trend in stiffness values with respect to seed spacing. As shown in Figure 2(c,d), 10-turn seeded springs were quite columnar, and, therefore, more prone to buckling as the degree of intertwining between springs decreased significantly for 1500 nm seed spacing, Figure 3(d).

Cross-sectional images prepared by ion-milling revealed spring tilting at stresses higher than 15 MPa. Figures 19(a,b) show two samples subjected to different stress levels, which demonstrated coordinated tilting of all springs in the same direction as indicated by the arrows. However, uncapped spring films demonstrated tilt in random directions. In addition to tilting of springs at stresses higher than 15 MPa, the capping layer of films comprised of 10-turn springs with 1500 nm spacing showed signs of fragmentation which was also reflected in jumps in the load vs. displacement curves. The capping layer was intact for the rest of the spring film types, apart from some “chipping” at the edges of the test areas. In general, uncapped films of unseeded films maintained their cohesion in the entire loading range due to major intertwining, Figure 20, films comprised of 4-turn springs and 1500 nm seed spacing showed moderate tilting, Figure 21, and, finally, 10-turn springs and 1500 nm seed spacing demonstrated pronounced spring tilting, especially at the test area edges, Figure 22.

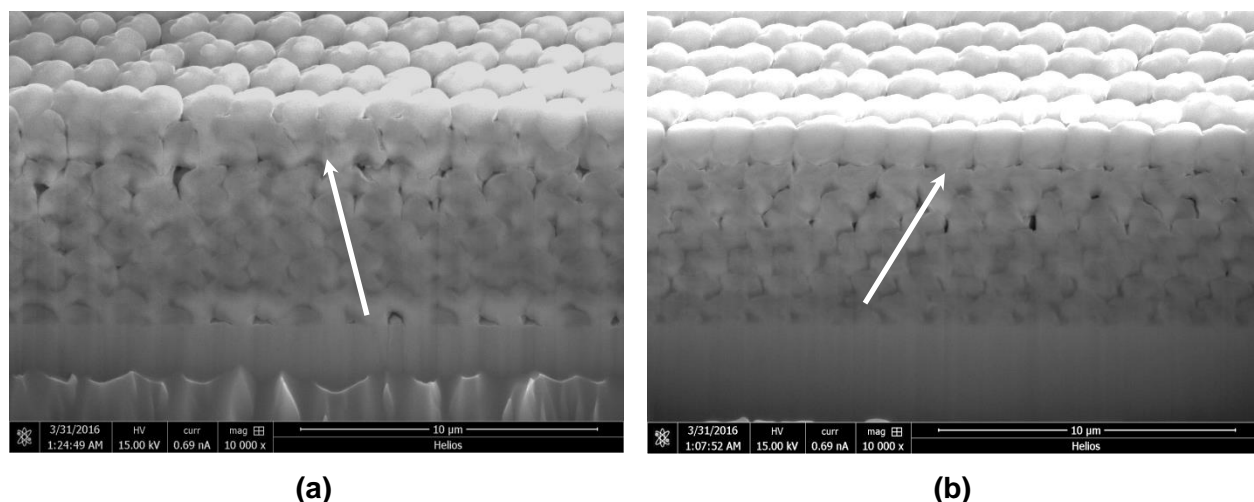


Figure 19. Cross-sectional images of capped films with 10-turn springs and 1500 nm seed spacing after subjected to **(a)** 15 MPa and **(b)** 25 MPa. The arrows show the tilt direction of the springs.

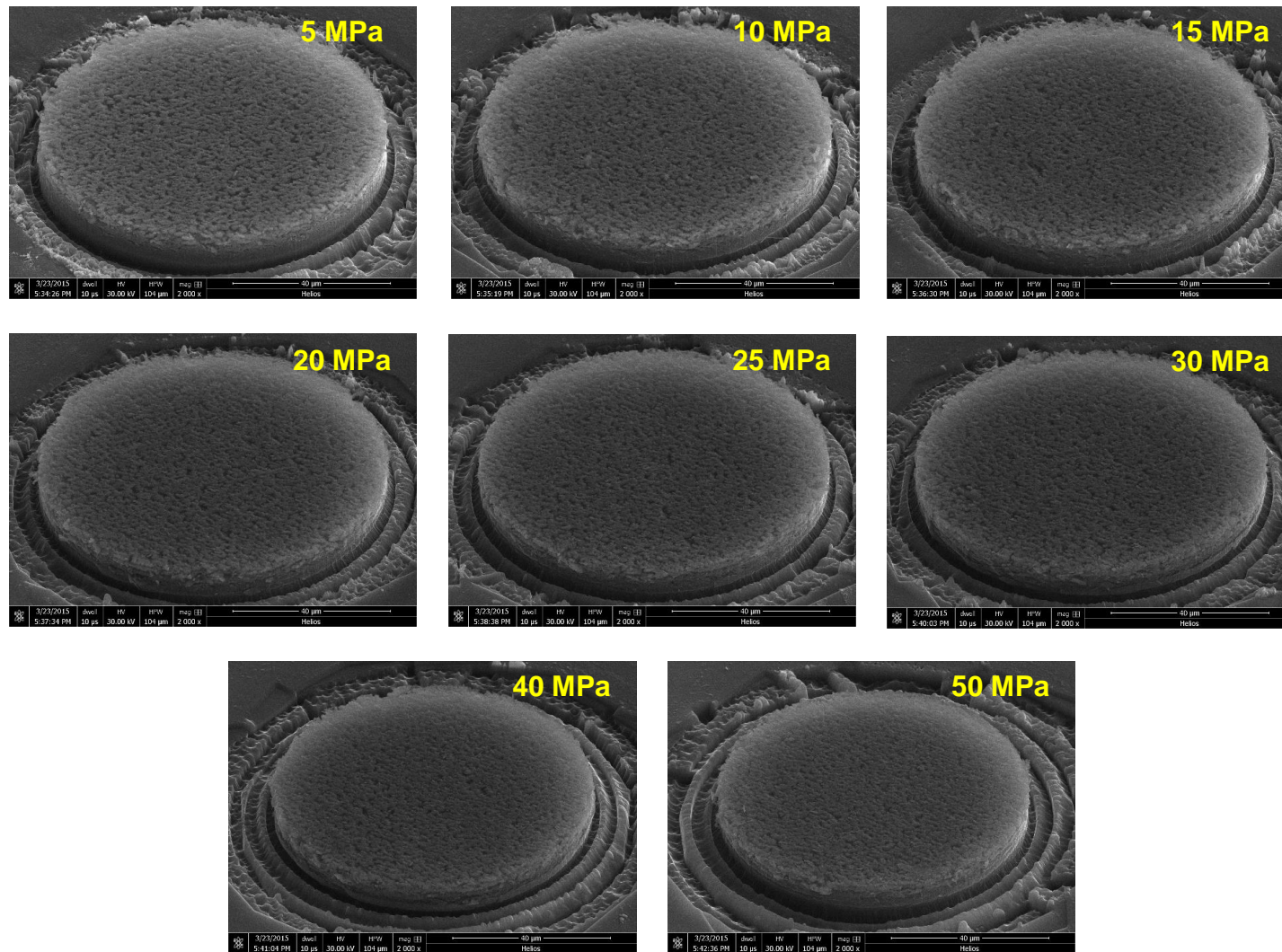


Figure 20. Oblique views of Si films comprised of unseeded springs with 4-turn coils, which were subjected to compressive stress in the range 5 MPa to 50 MPa.

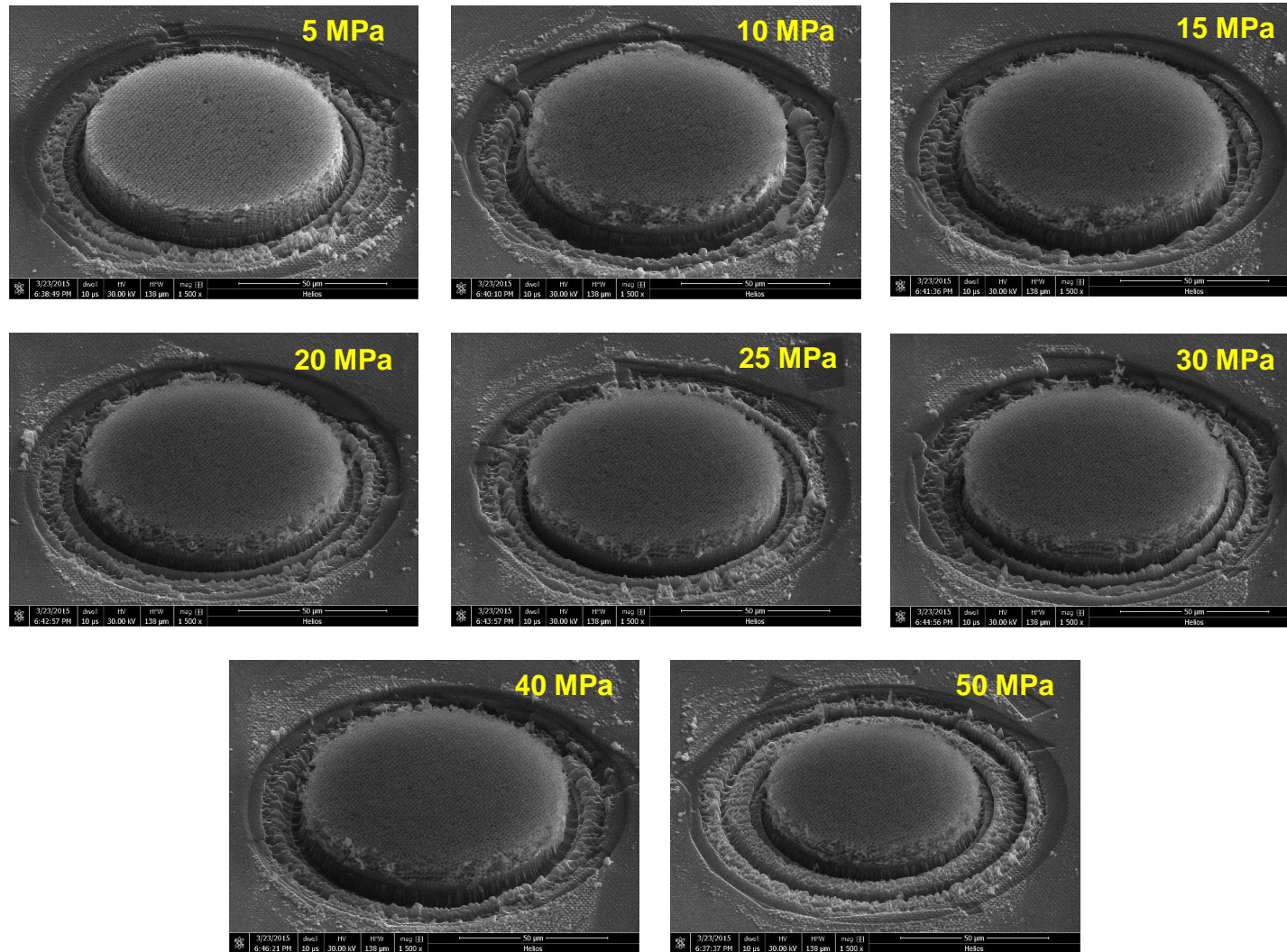


Figure 21. Oblique views of Si films comprised of 4-turn coils with 1500 nm seed spacing, which were subjected to compressive stress in the range 5 MPa to 50 MPa.

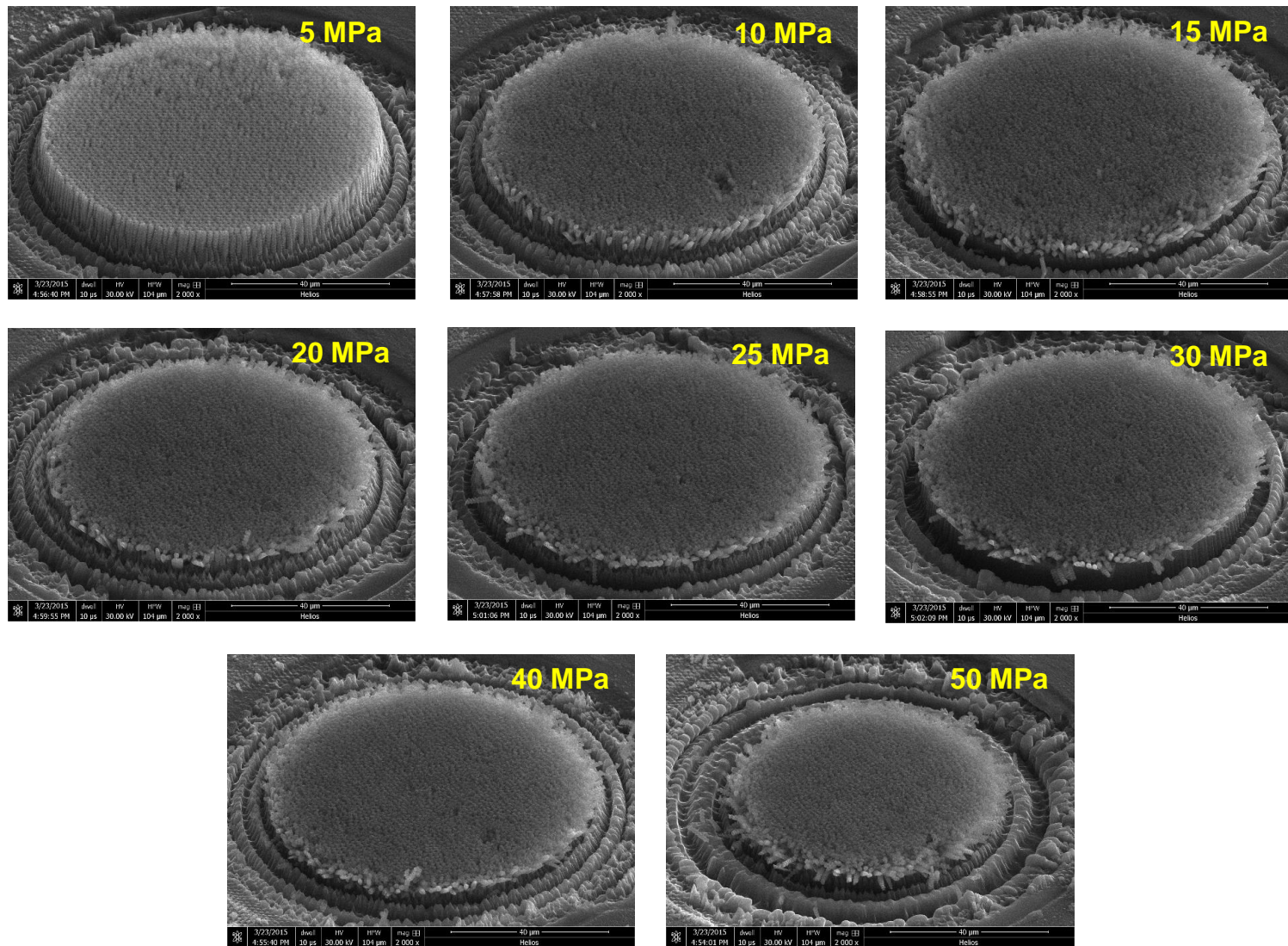


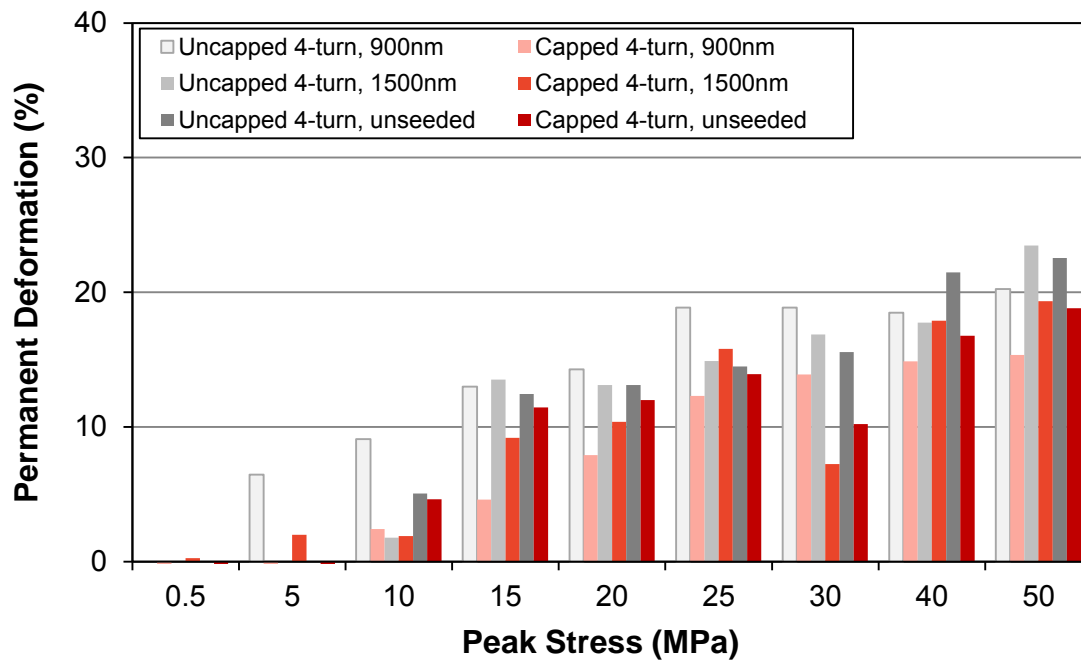
Figure 22. Oblique views of Si films comprised of springs with 10-turn coils and 1500 nm seed spacing, which were subjected to compressive stress in the range 5 MPa to 50 MPa.

The final film thickness was divided by the initial film height to determine the permanent deformation (strain). Figures 23(a,b), and Figures 24(a,b) in logarithmic coordinates, show the permanent set of all Si films tested in this research program. Si films comprised of 4-turn coils with 900 nm seed spacing and 10-turn coils with 1500 nm seed spacing sustained a permanent strain of 6.5% and 1.9%, respectively, at 5 MPa. In all other cases, a permanent strain between 0.6% and 5.1% took place for the first time at 10 MPa. For example, capped Si films with 4-turn coils and 1500 nm seed spacing, and 10-turn coils with 1500 nm seeding had 2.0% and 1.9% permanent strain, respectively, upon application of 5 MPa stress.

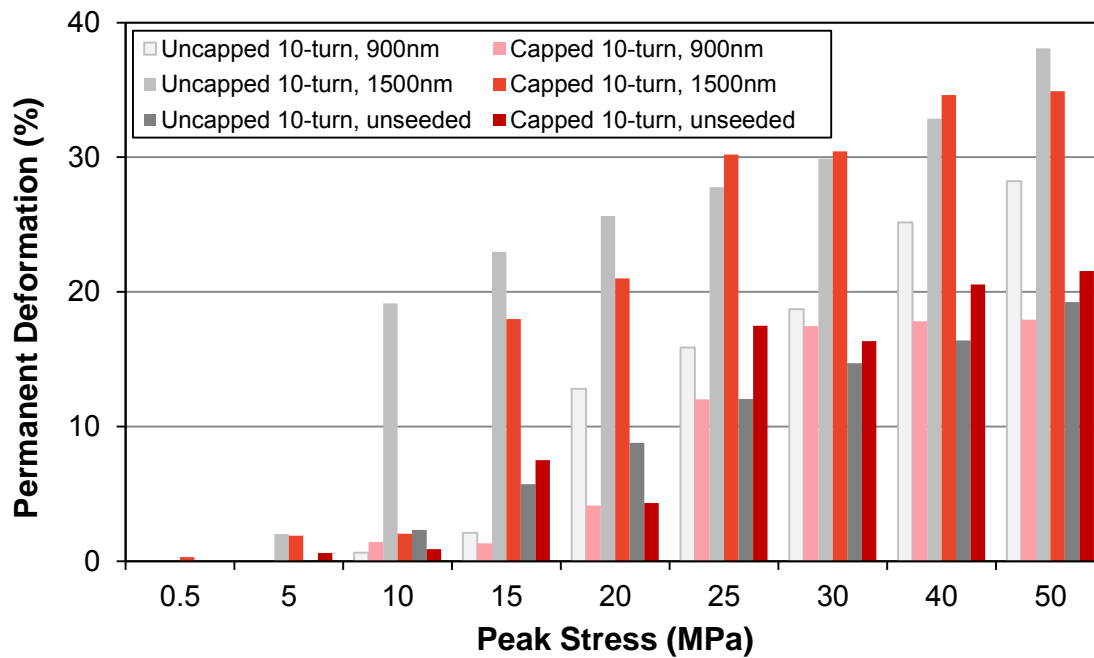
Between 15 MPa and 30 MPa applied stress, all uncapped 4-turn films experienced comparable permanent strain regardless of seed spacing, which varied in the range 12.4% - 18.9%. Notably, the permanent strain of films with 900 nm seed spacing remained rather unchanged at 18-20% for stresses \geq 25 MPa. At intermediate stresses of 15-30 MPa unseeded films demonstrated the most resistance to permanent compression with 12-16% permanent strain, which increased abruptly to 21.5% and 22.5% at 40 MPa and 50 MPa, respectively. On the other hand, 10-turn spring films showed steady increase in permanent strain with applied stress. Uncapped films of 10-turn springs and 1500 nm seed spacing, although experienced only 2.0% permanent strain at 5 MPa, Figure 23(b), their permanent strain increased to 19% at 10 MPa, and then increase thereafter by 2-3% for each 5 MPa of stress increment, finally reaching 38% at 50 MPa.

On the contrary, films of 10-turn springs with 900 nm seed spacing and unseeded films subjected to 5 MPa incurred permanent strains of 0.6% and 2.3%, respectively. For stresses lower than 15 MPa, films of springs with 900 nm spacing were proven to be the most resistant to permanent deformation. A drastic increase in permanent compression occurred for films with 10-turn coils and 900 nm seed spacing from 2% at 15 MPa to \sim 13% at 20 MPa. Films with 10-turn unseeded springs demonstrated the most consistent increase in permanent strain of 2-3% for each 5 MPa of stress increment, reaching 19% permanent strain at 50 MPa. The permanent strain in 10-turn spring films varied greatly depending on the seed spacing: films with 1500 nm seed spacing demonstrated the largest permanent strain, followed by those with 900 nm seed spacing and finally the unseeded springs. Therefore, unseeded films provided a clear advantage in the case of 10-turn springs, but limited advantage in 4-turn spring.

For stresses between 15 MPa and 25 MPa, capped films of 4-turn coils and 900 nm seeding had 4.6% - 12.3% permanent deformation which further increased to 17.1% at 50 MPa. In the same range of stresses (15-25 MPa) capped 4-turn spring films with 1500 nm seed spacing showed slightly larger permanent deformation of 9.2% - 15.8%, which reached 19.3% at 50 MPa. The unseeded capped films with 4-turn coils, on the other hand, *had larger permanent deformation* of 11.5% - 13.9% between 15 MPa and 25 MPa and 22.5% at 50 MPa. 10-turn spring films demonstrated similar trends with permanent deformation varying anywhere between 1.3% and 30.2% for stresses between 15 MPa and 25 MPa. At 50 MPa, capped films of 10-turn coils with 900 nm seed spacing had 17.9% permanent strain, those with 1500 nm seed spacing had 34.9% permanent set, and unseeded films had 21.5% permanent strain. Capped films with 10-turn coils and 1500 nm seeding exhibited the largest permanent deformation among all types of films, which was the outcome of the lack of stabilizing lateral interactions between the adjacent springs, leading to spring tilting. Finally, capped films, especially for 10-turn coils provide a clear advantage as they limit the amount of permanent deformation compared to uncapped films.

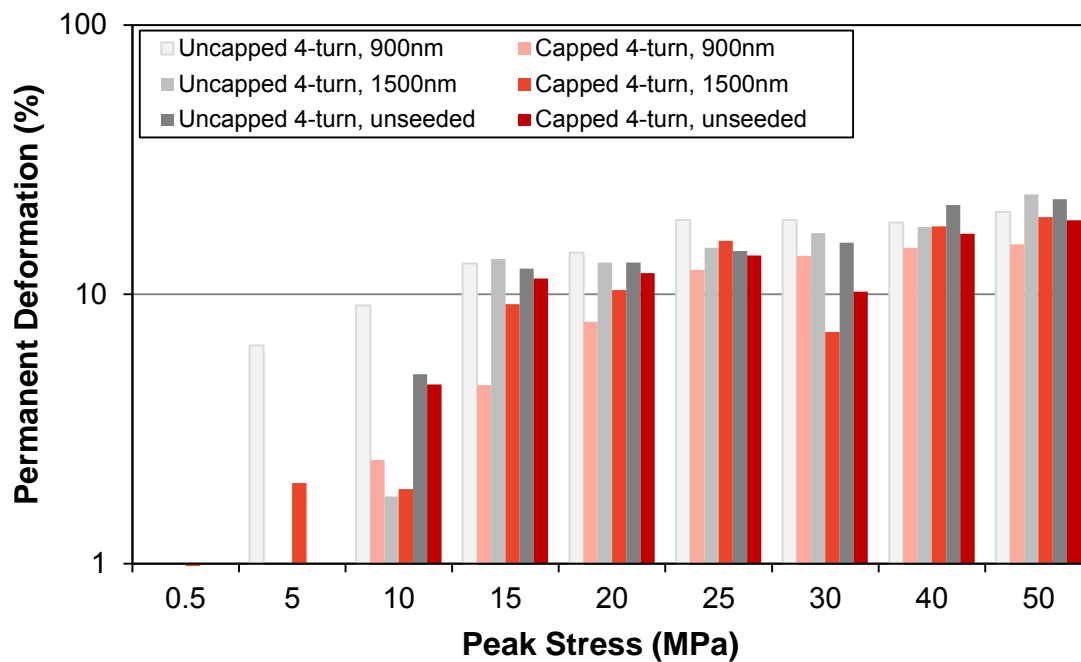


(a)

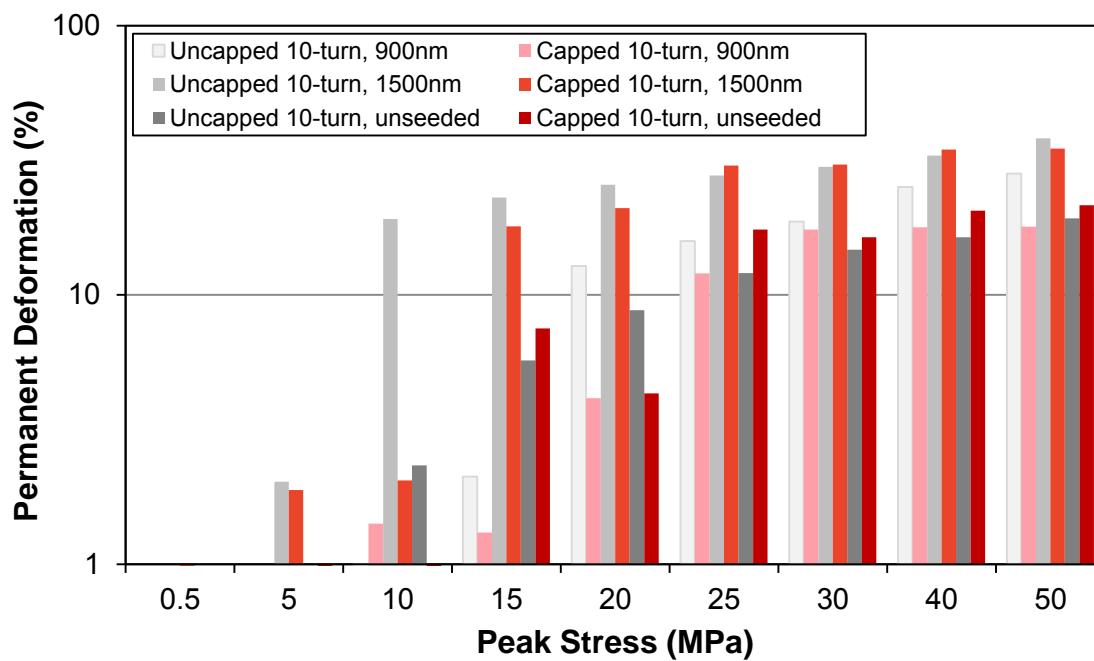


(b)

Figure 23. Permanent strain of uncapped and capped Si films with (a) 4-turn, and (b) 10-turn springs.



(a)



(b)

Figure 24. Permanent strain of uncapped and capped Si films with (a) 4-turn, and (b) 10-turn springs. The data are the same as in Figure 23, presented here in logarithmic scale for better definition of the permanent deformation values at low stresses.

III.2 Shear Response of Si Spring Films

The shear modulus of different films, as determined via Equation (3), is reported in Figure 25. The standard deviation for each case is calculated from three different experiments, except for the case of unseeded films, for which stiffness is extracted from two tests. With the exception of films comprised of 10-turn springs with 1500 nm spacing, the shear modulus of all other films was in the tight range between 16.8 ± 1.8 MPa and 26.8 ± 7.1 MPa. The difference in the shear modulus values between different types of films was due to their dimensions and the degree of entanglement. As listed in Table 1, the 4-turn springs with 1500 nm spacing had larger wire diameter than the 4-turn springs with 900 nm seed spacing and as a result larger stiffness. On the other hand, unseeded springs with 4 turn coils had among the highest shear stiffness values measured: As shown in Figures 2(a-f), unseeded springs formed much denser films compared to seeded films, hence promoting significantly more intertwining and lateral interactions through contact. Therefore, unseeded films were expected to have comparatively higher shear stiffness than seeded films. Films with 10-turn springs did not follow monotonic trends in shear stiffness and strength: Films of 10-turn coils with 900 nm seeding and 10-turn coils with 1500 nm seeding had shear stiffness values of 26.1 ± 4.7 MPa and 6.6 ± 0.6 MPa, respectively. Although the latter had larger effective wire diameter, there were fewer springs per unit area than in the former case, as well as almost no intertwining to resist spring tilting. For these reasons films of 10-turn coils and the largest seed spacing had the smallest shear stiffness. On the other hand, unseeded films with 4-turn coils were the stiffest (26.8 ± 7.1 MPa), while, films with unseeded 10-turn springs were comparably stiff (23.5 ± 3.2 MPa) due to the closest proximity of adjacent unseeded springs. Notably, compared to seeded films, *unseeded films had reduced compressive stiffness but equivalent or higher shear stiffness.*

In terms of shear strength, Figure 26, all 4-turn spring films demonstrated similar shear strength regardless of seed spacing, amounting to 2.4 ± 0.2 MPa, 2.4 ± 0.1 MPa, and 2.3 ± 0.1 MPa, for 900 nm seeding, 1500 nm seeding and unseeded films, respectively. As a consequence of the deposition process of GLAD, films with larger seed spacing had larger coil and wire cross-sections, but fewer springs than those with smaller seed spacing. Therefore, although the individual spring geometries varied greatly, the film shear strengths were quite consistent. Films with 10-turn coils demonstrated less consistent behavior: films with 10-turn coils and 900 nm seed spacing and unseeded films had similar shear strength, namely 3.2 ± 0.5 MPa and 3.9 ± 0.7 MPa, respectively. However, films of 10-turn coils with 1500 nm seed spacing had low shear strength, only 0.9 ± 0.05 MPa for the reasons explained above. It is worth mentioning that seeded films of 4-turn springs failed randomly along the spring height anywhere between the first and the fourth turn. On the other hand, unseeded 4-turn springs experienced failure consistently between the third and the fourth turn. However, 10-turn seeded springs experienced failure exclusively at the post, whereas 10-turn unseeded springs failed either near the base or the cap.

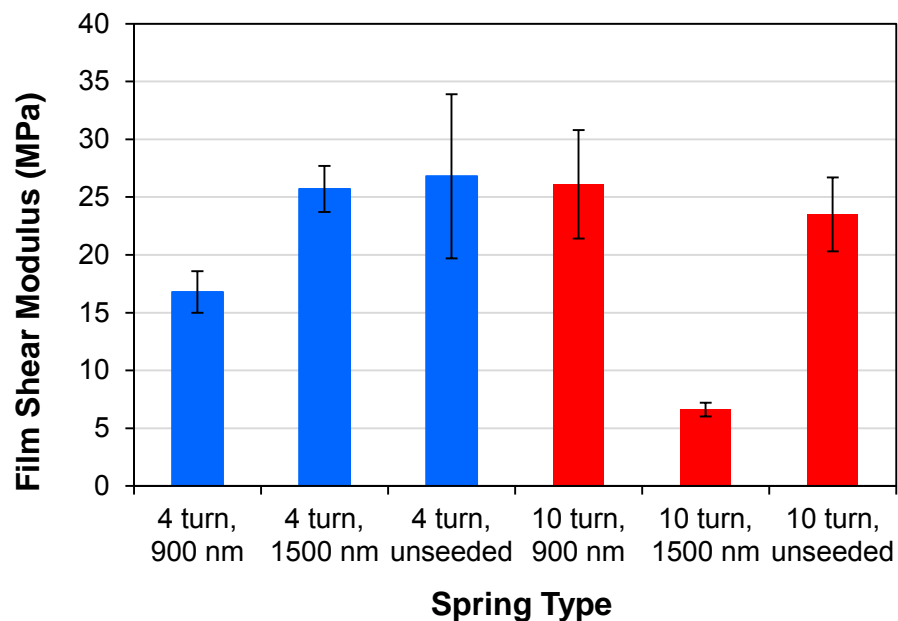


Figure 25. Shear stiffness of unseeded and seeded Si spring films.

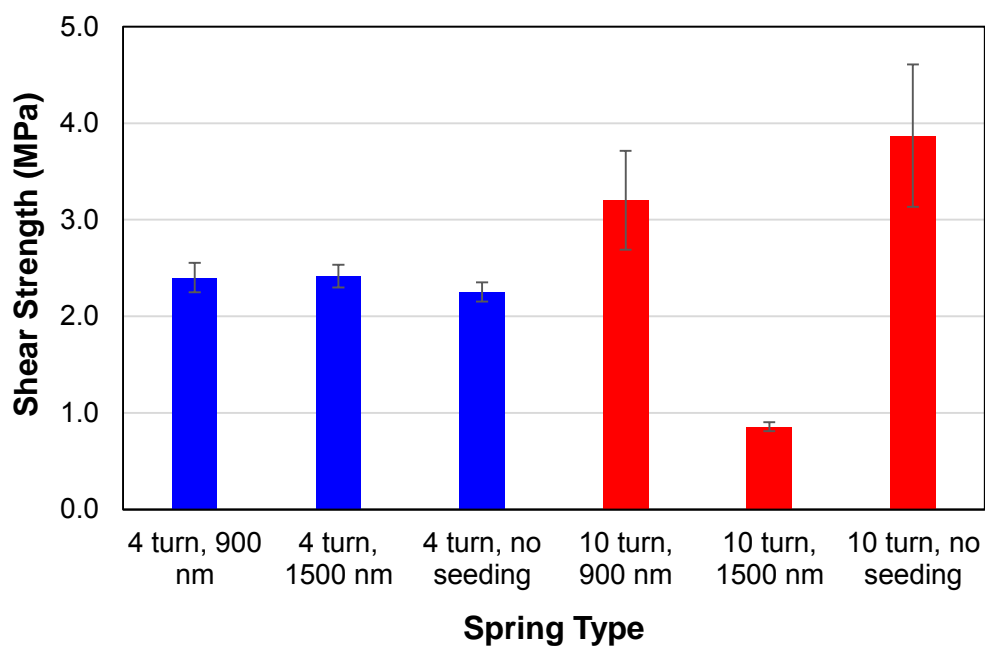


Figure 26. Ultimate shear strength of unseeded and seeded Si spring films.

III.3 Compressive Behavior of Cu Spring Films

A comparison of the unloading stiffness of the different types of Cu spring films is provided in Figure 27. The stiffness of Cu films with 2400 nm, or 2800 nm seed spacing gradually increased with the magnitude of applied stress, ranging from 509 ± 16.8 MPa and 560 ± 19.8 MPa, respectively, at 5 MPa stress, to 4613 ± 149 MPa and 2795 ± 58.4 MPa, respectively, at 50 MPa. However, the compressive stiffness of films with 2000 nm and 3200 nm seed spacing monotonically increased up to 30 MPa stress, reaching 3512 ± 185 MPa and 2915 ± 107 MPa, respectively. Notably, the stiffness of both types of films decreased when the stress increased from 30 to 40 MPa, slightly for springs with 2000 nm seed spacing to 3138 ± 100 MPa, but drastically for films with 3200 nm seed spacing to 1751 ± 26.4 MPa. In the stress increment between 40 to 50 MPa, the film stiffness increased again for both spring types, to 3797 ± 124 MPa for films with 2000 nm seed spacing, and to 1863 ± 27.5 MPa for films with 3200 nm seed spacing. The stiffness of unseeded films was 250 ± 4.9 MPa at 5 MPa, and increased steadily to 613 ± 6.8 MPa and 627.5 ± 7.9 MPa for 20 MPa and 30 MPa, respectively. A further increase in stress from 30 to 40 MPa produced a more drastic stiffness increase to 1121 ± 18.4 MPa, but no further increase occurred when the stress increased to 50 MPa, suggesting that between 30 and 40 MPa, the degree of contact between adjacent springs was substantially greater than it was between 20 and 30 MPa, and perhaps reached saturation at 40 MPa. Unseeded Cu films demonstrated the smallest stiffness at all stress levels, only reaching 1 GPa at 40 and 50 MPa. For stresses ≤ 25 MPa, the compressive stiffness of all film types was less than 3 GPa, which is 40 times less than bulk Cu. At stresses smaller or equal to 25 MPa, films with 3200 nm seed spacing had the largest stiffness among all samples, due to their largest coil and wire diameter. At higher stresses, the reduction in stiffness of the films with the largest Cu coils was due to the cork-screw shape of the springs, which promoted tilting and shifting instead of spring-like compression. On the other hand, Cu coils with 2000 nm seed spacing better resembled coils and, thus, demonstrated more uniform change in stiffness with applied stress, only to be limited by the onset of interactions between interpenetrating adjacent springs. In general, *seeded Cu springs with seed spacings of 2000-2800 nm demonstrated monotonic and thus controllable stiffening* with applied stress, while unseeded Cu films were by far the most compliant of all types of films tested.

The films of Cu springs resisted permanent deformation more than the Si films discussed in previous Sections. In the case of Cu films, each test area deformed uniformly, and the springs at the specimen edges did not tilt outwards as in the case of Si films. The permanent set of Cu films, Figure 28, was calculated from SEM images captured before and after testing. For Cu films with 2000 nm and 2800 nm seed spacing, $\sim 2\%$ permanent strain occurred first at 20 MPa, while in all other films, the first occurrence of permanent strain was recorded at 25 MPa and varied between 1% for unseeded films to 2% for films with 2400 nm and 3200 nm seed spacing. Unseeded films of Cu springs experienced large permanent set of 10.4% strain at 30 MPa, but at higher stresses, the rate of change in permanent set decreased significantly, reaching 12% at 50 MPa. Seeded films experienced consistently increasing permanent set with applied stress. At 50 MPa, the permanent set of films with 2000 nm and 3200 nm seed spacing was 8%, and 6%, respectively. Thus, *although unseeded films provided the highest compliance, they were more prone to permanent deformation at high stresses compared to seeded Cu films.*

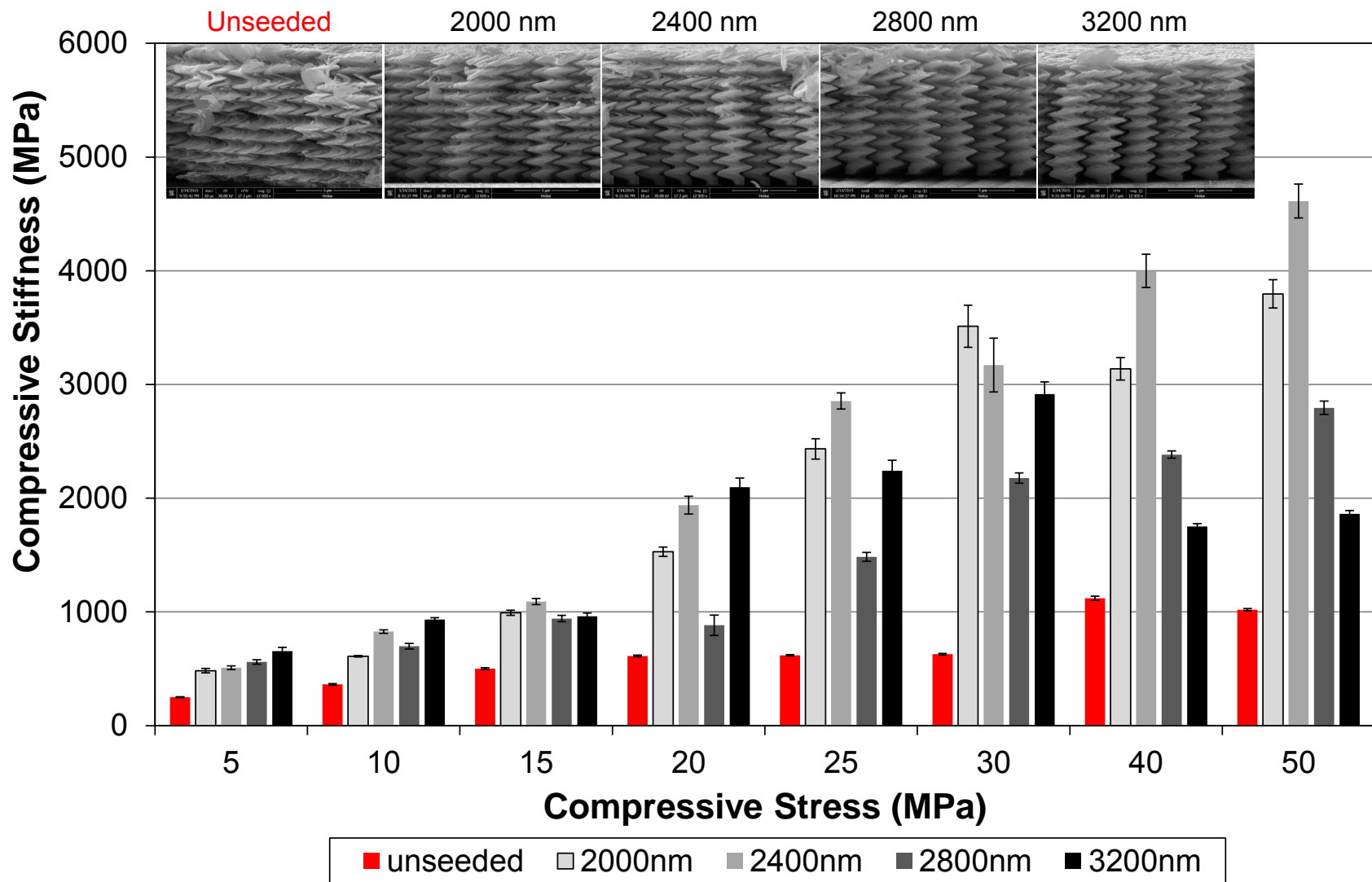


Figure 27. Compressive unloading stiffness of unseeded (red) and seeded (gray) Cu spring films.

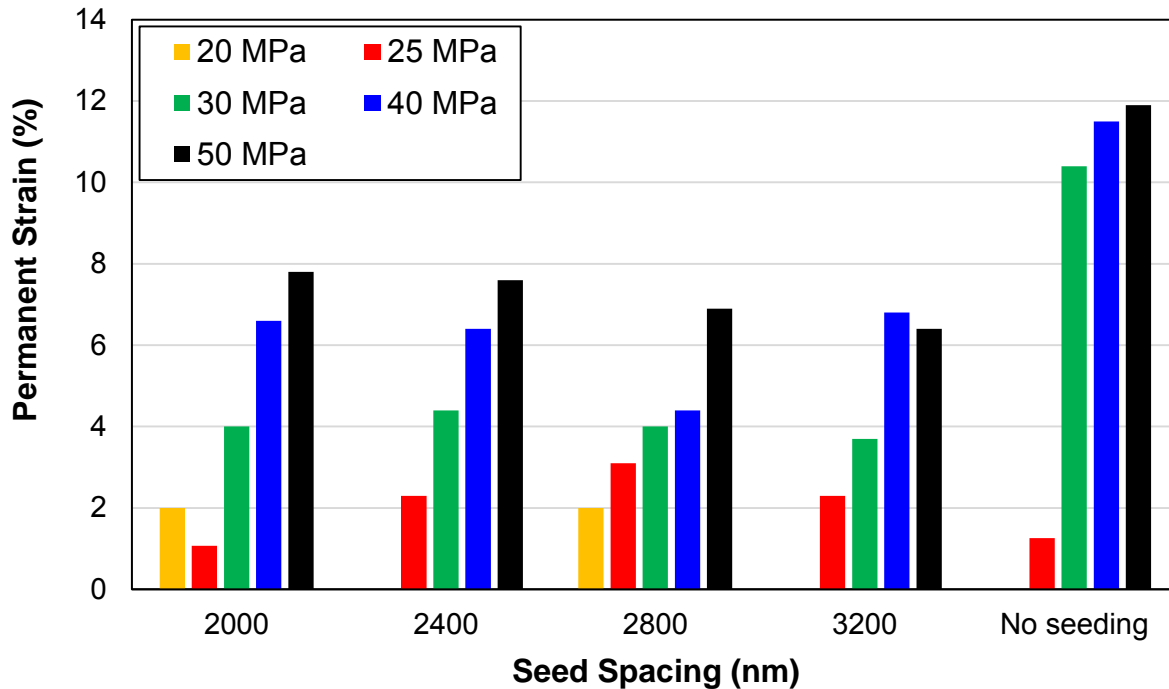


Figure 28. Permanent compressive strain of unseeded and seeded Cu spring films.

III.4 Shear Behavior of Cu Spring Films

As shown in Figure 29, all Cu spring films had shear stiffnesses that varied between 218 and 322 MPa with no discernible trend. The similar stiffness values were due to the inverse relationship between seed spacing and the resulting spring density. Larger seed spacings resulted in larger spring features, such as wire and coil diameter, but smaller number of springs per film unit area, compared to films with smaller seed spacing. Also, the effect of spring intertwining is important: Films with smaller seed spacing had more spring overlap, and thus, came into contact at smaller shear displacements compared to springs with larger seed spacing.

The ultimate shear strength values of seeded Cu films, shown in Figure 30, were quite similar: films with 2000 nm seed spacing had the largest strength of 4.1 ± 1.2 MPa, while films with 2400 nm seed spacing had the lowest strength of 1.8 ± 0.4 MPa. The shear strengths of films with 2800 nm and 3200 nm seed spacing were 2.6 ± 0.4 MPa and 3.9 ± 0.4 MPa, respectively. Unseeded films had much greater shear strength, reaching 16.1 ± 0.9 MPa, compared to all seeded films. Seeded springs were deposited on narrow posts compared to the coil diameter, which provided a weak location for failure under shear loading. Thus, *unseeded Cu films provide the best performance in shear*. Improvements in bonding Cu springs onto their seeds are needed to offset this disadvantage.

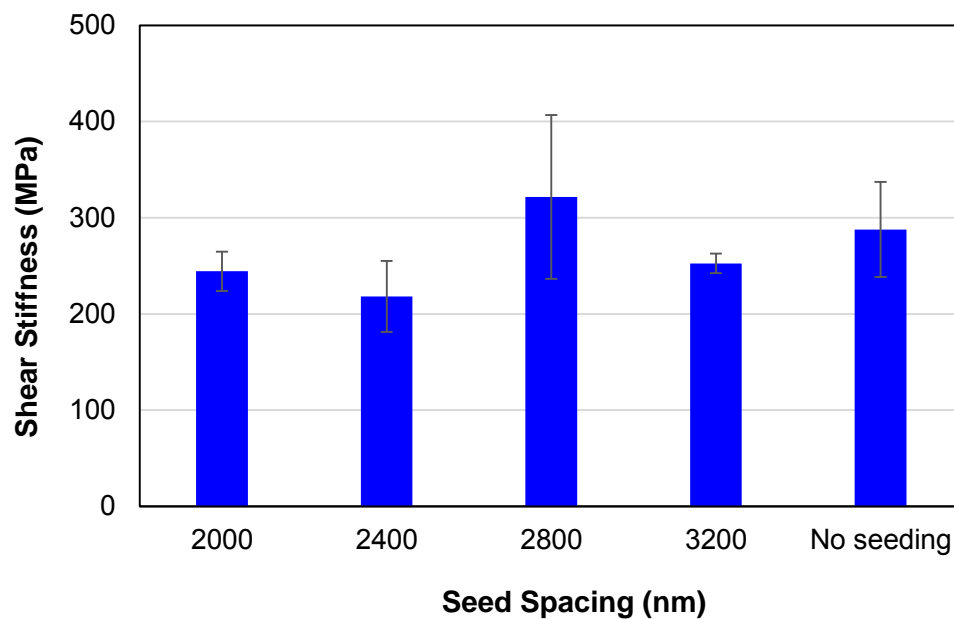


Figure 29. Shear stiffness of unseeded and seeded Cu spring films.

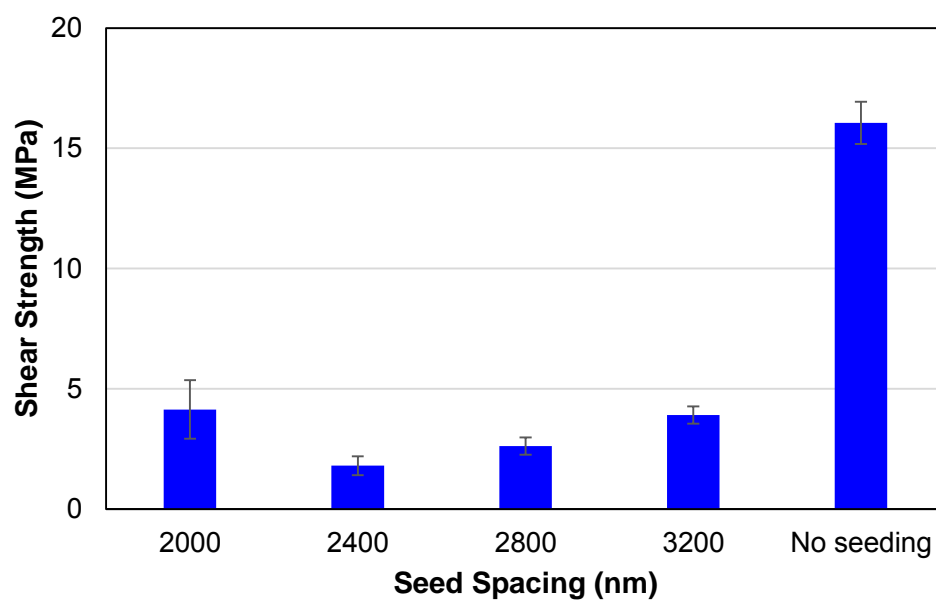


Figure 30. Ultimate shear strength of unseeded and seeded Cu spring films.

III.5 Mechanical Behavior of Individual Si Nanosprings

III.5.1. Tension/Compression and Shear Behavior of Individual Si Springs

The tension and compression experiments of individual springs using MEMS devices provided force-extension/compression curves which were used to compute the initial stiffness of individual springs. Figures 31(a-d) and Figures 32(a-d) show the load vs. spring extension/compression graphs of four different types of springs subjected to tension and compression, respectively. Note that depending on specimen mounting the lengths of the specimens whose force-extension curves are shown in this section were not the same, therefore the slopes of the curves in these plots cannot be compared directly. Under tension, springs with 4 turns behaved mostly linearly. Springs with 10 turns were also linear in the beginning of loading; springs from films with 1500 nm seed spacing, which resembled cork screws, e.g. Figure 2(d), demonstrated the most non-linearity in tension.

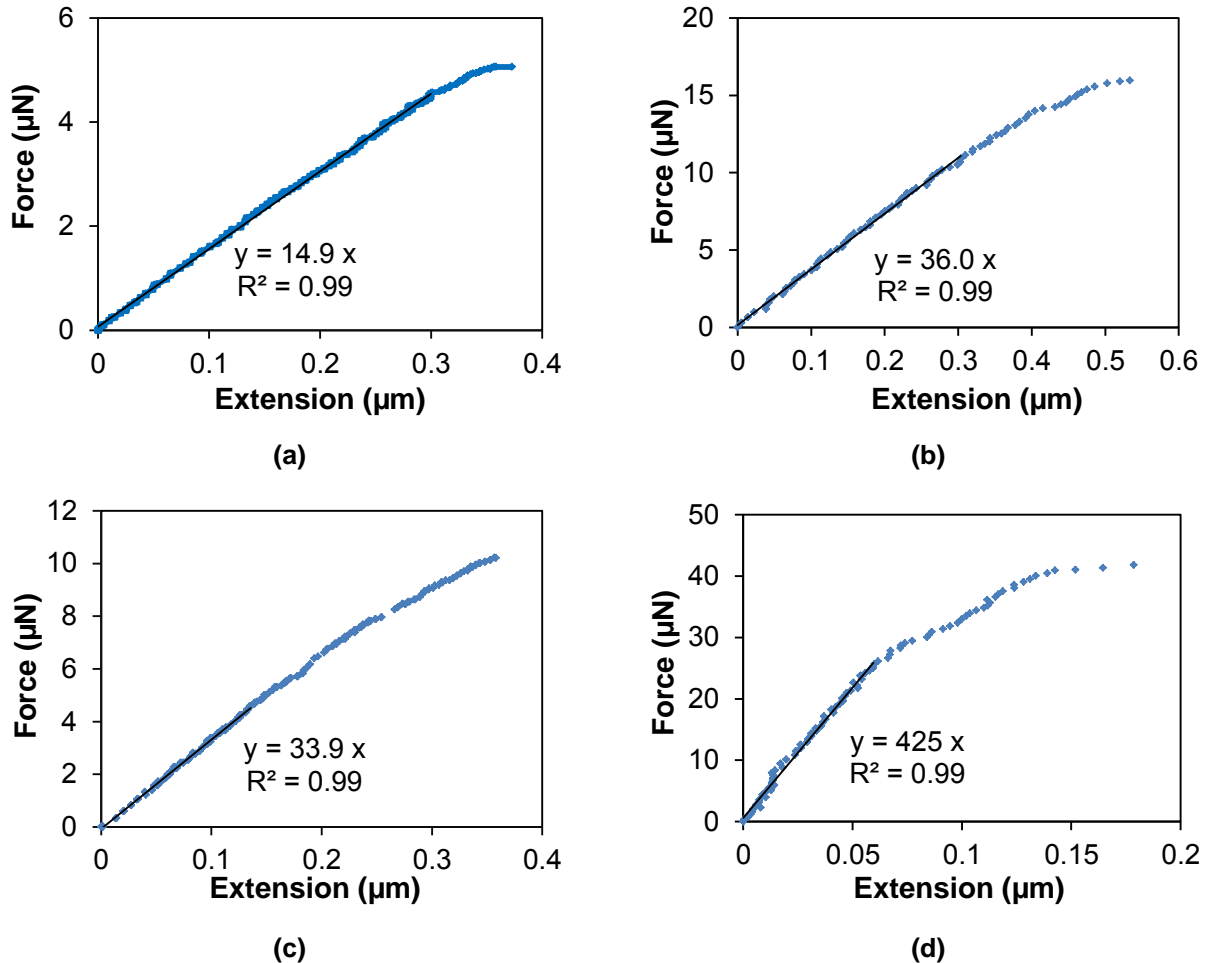


Figure 31. Force vs. extension of individual Si springs from films with (a) 4-turn coils and 900 nm seed spacing, (b) 4-turn coils and 1500 nm seed spacing, (c) 10-turn coils and 900 nm seed spacing and (d) 10-turn coils and 1500 nm seed spacing. The initial slope of each curve is also shown. Depending on specimen mounting the gauge length differed between specimens.

Contrary to the tension results in Figure 31, all individual springs subjected to compression behaved non-linearly after an initial linear segment, potentially due to progressive bending (buckling due to initial imperfection due to the coil geometry). Under tension, the average initial stiffness was 7.7 ± 1.8 N/m, 18.5 ± 3.7 N/m, 19.2 ± 1.2 N/m and 215 ± 88 N/m for springs from films comprised of 4-turn coils with 900 nm seeding, 4-turn coils with 1500 nm seeding, 10-turn coils with 900 nm seeding, and 10-turn coils with 1500 nm seeding, respectively, all corrected for a 10- μm long springs. For the same types of springs the initial compressive stiffness was 7.3 ± 2.1 N/m, 17.0 ± 1.5 N/m, 32.7 ± 6.7 N/m and 187 ± 19 N/m, respectively. Figure 33 shows a comparison between experimental measurements and the analytical models described by Equations (4-10). As shown, springs with 4 turns were the closest to theoretical predictions while springs with 10 turns deviated from the ideal spring behavior. It should be noted *that analytical estimates are very sensitive to the geometry of the coil wire which was determined from SEM images similar to those in Figures 9(a,b), which can suffer from perspective errors. Improved measurements are in progress, taking into account the growth dynamics of the GLAD process when calculating the precise shape of the springs.*

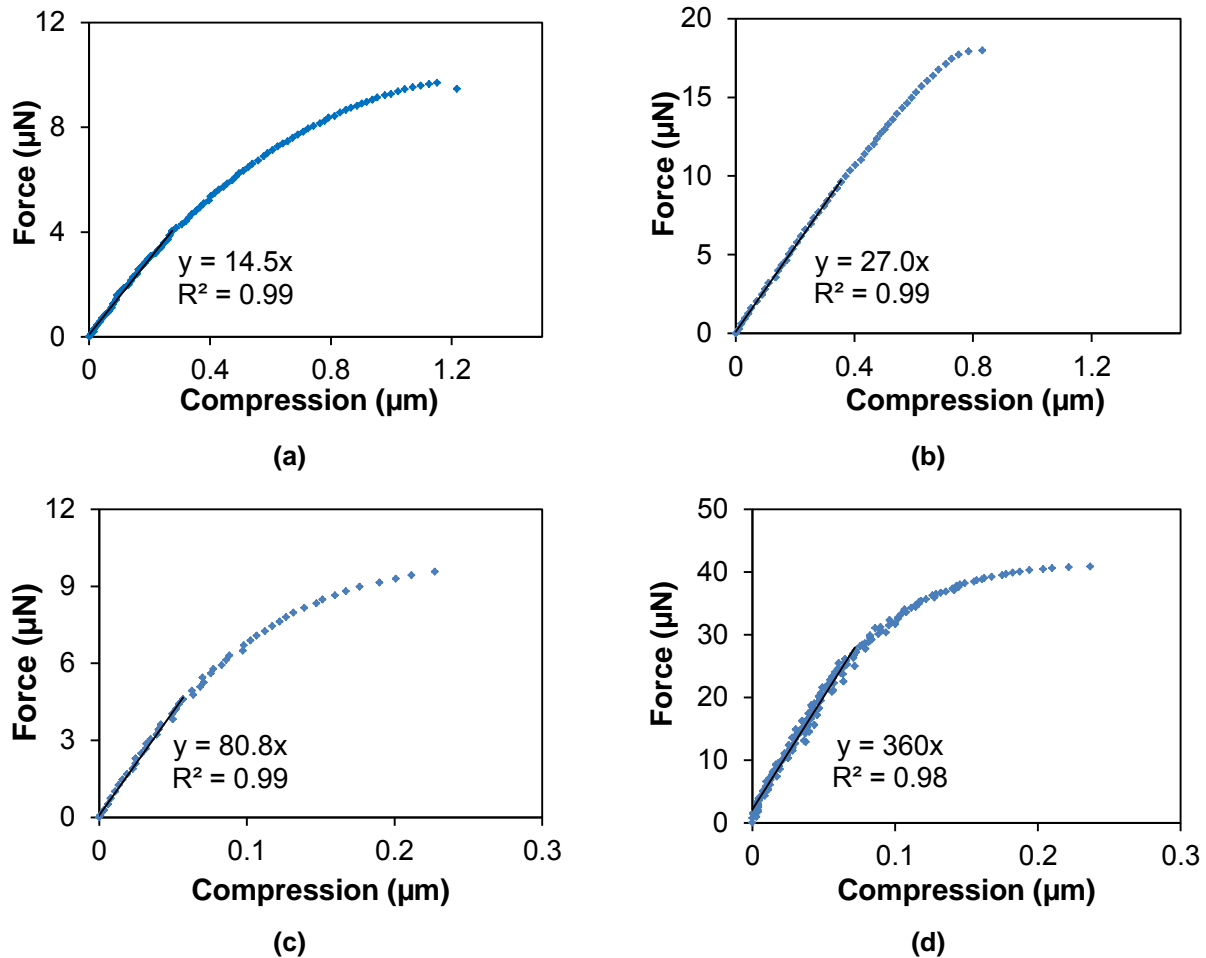


Figure 32. Load vs. compression of individual Si springs from films with (a) 4-turn coils and 900 nm seed spacing, (b) 4-turn coils and 1500 nm seed spacing, (c) 10-turn coils and 900 nm seed spacing and (d) 10-turn coils and 1500 nm seed spacing. The initial slope of each curve is also shown. Depending on specimen mounting the gauge length differed between specimens.

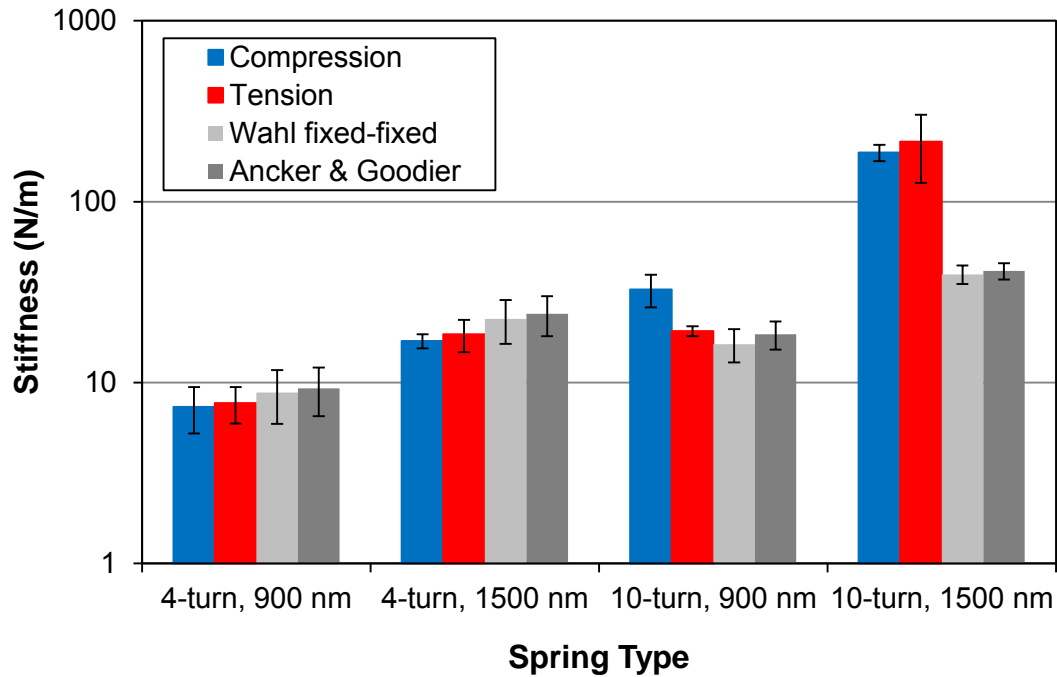


Figure 33. Comparison between measured stiffness of individual Si springs in tension and compression and analytical model predictions using Wahl's and Ancker and Goodier's models. All stiffness values refer to 10- μ m long springs. Note that the scale is logarithmic to ensure that all results are shown properly in the same graph.

The reliability of individual spring measurements lies with the rigidity of the Pt tabs deposited with a FIB, which was assessed after testing of each spring, and confirmed the rigid bonding of the tested springs. Figures 34(a,b) show the failure segments of a spring from a film comprised of 4-turn coils and 900 nm seed spacing after tensile testing.

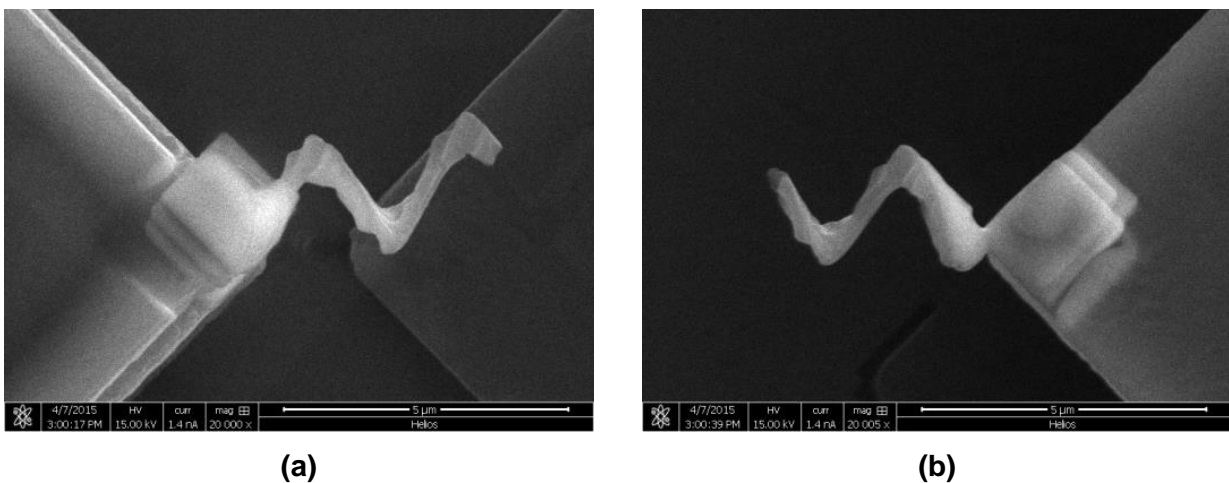


Figure 34. Failure segments of a 4-turn Si spring from a film with 900 nm seed spacing, subjected to tensile loading.

Bending (shear) tests of individual springs provided the force vs. bending deflection curves as a function of spring geometry. Figures 35(a-d) show characteristic force vs. deflection plots for each type of seeded Si springs. The transverse stiffness of individual Si springs under bending (shear) loading was 1.8 ± 1.0 N/m for 4-turn coils (900 nm seed spacing), 5.1 ± 2.1 N/m for 4-turn coils (1500 nm seed spacing), 2.4 ± 1.0 N/m for 10-turn coils (900 nm seed spacing), and 20.1 ± 10.2 N/m for 10-turn coils (1500 nm seed spacing). Note that depending on specimen mounting the lengths of the specimens whose curves are shown in Figures 35(a-d) were not the same, thus, the slopes of the curves cannot be directly compared. The average initial transverse (bending) stiffness exhibited large standard deviations, which may imply that the experimental results are sensitive to the precise orientation of the mounted springs onto the MEMS testing device with respect to their neutral axis. The force vs. bending deflection graphs of individual Si springs from films with 4-turn coils and 900 nm seed spacing, 4-turn coils and 1500 nm seed spacing, and 10-turn coils and 900 nm seed spacing were linear, whereas the graphs of springs with 10 turns from films with 1500 nm seed spacing demonstrated more non-linearity.

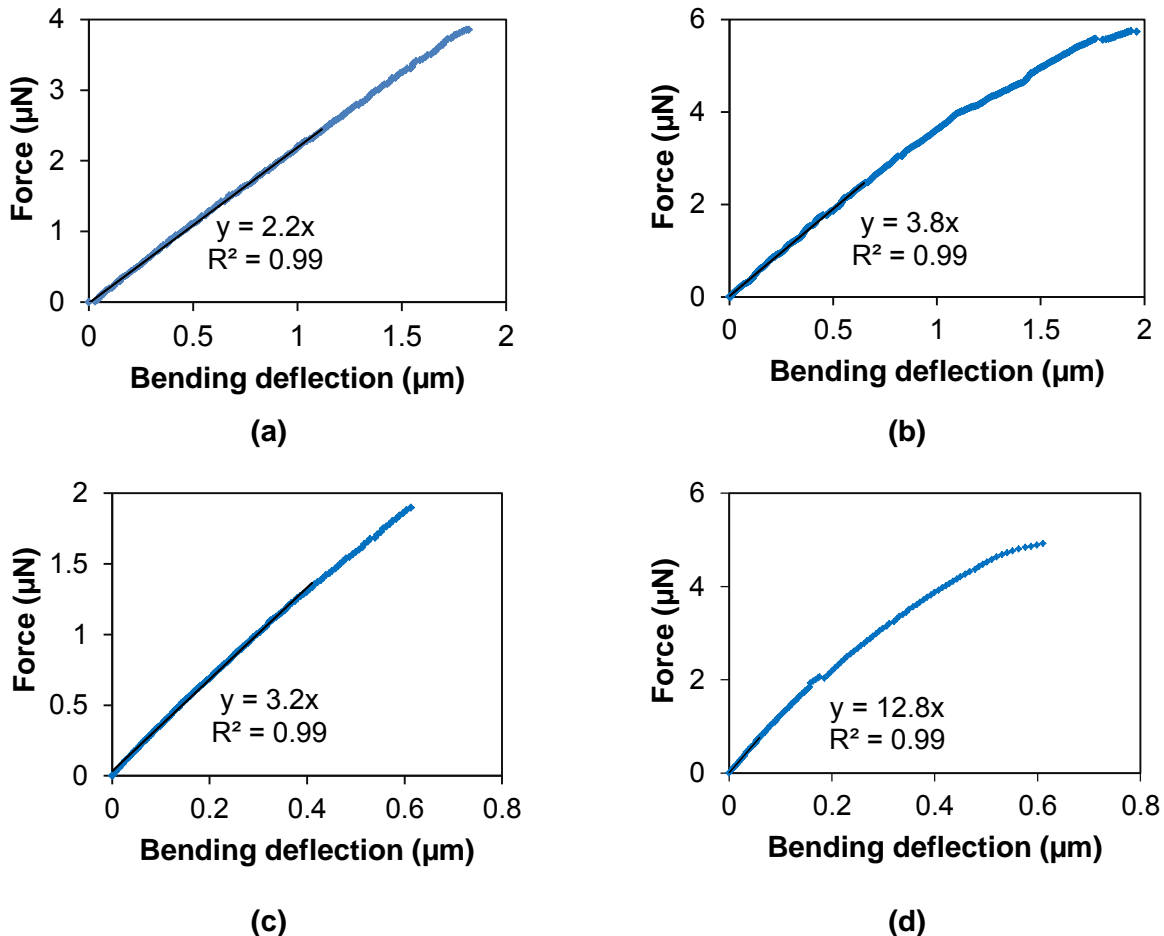


Figure 35. Load vs. deflection of individual Si springs from films with (a) 4-turn coils and 900 nm seed spacing, (b) 4-turn coils and 1500 nm seed spacing, (c) 10-turn coils and 900 nm seed spacing, and (d) 10-turn coils and 1500 nm seed spacing. The initial slope of each curve is also shown. Depending on specimen mounting the gauge length varied between specimens.

Figure 36(a) presents the bending stiffness results for different Si springs, originating in seeded films, which was adjusted for 10- μm gauge sections. These values, together with the area density of seeded spring films were used to estimate the shear stiffness of the films, which in turn were compared with the measured shear stiffness and shown in Figure 36(b). As shown in this figure, the estimates and measurements are in good agreement which implies that the contribution of lateral spring interactions was not as important for the small shear strains applied in our tests. Only the case of films with 10-turn springs with 1500 nm spacing was not predicted well from individual spring data; the particular estimated film shear stiffness value shown in Figure 36(b) is potentially more reliable than the experimental value, because of likely early debonding of these large Si coils that resembled cork-screws.

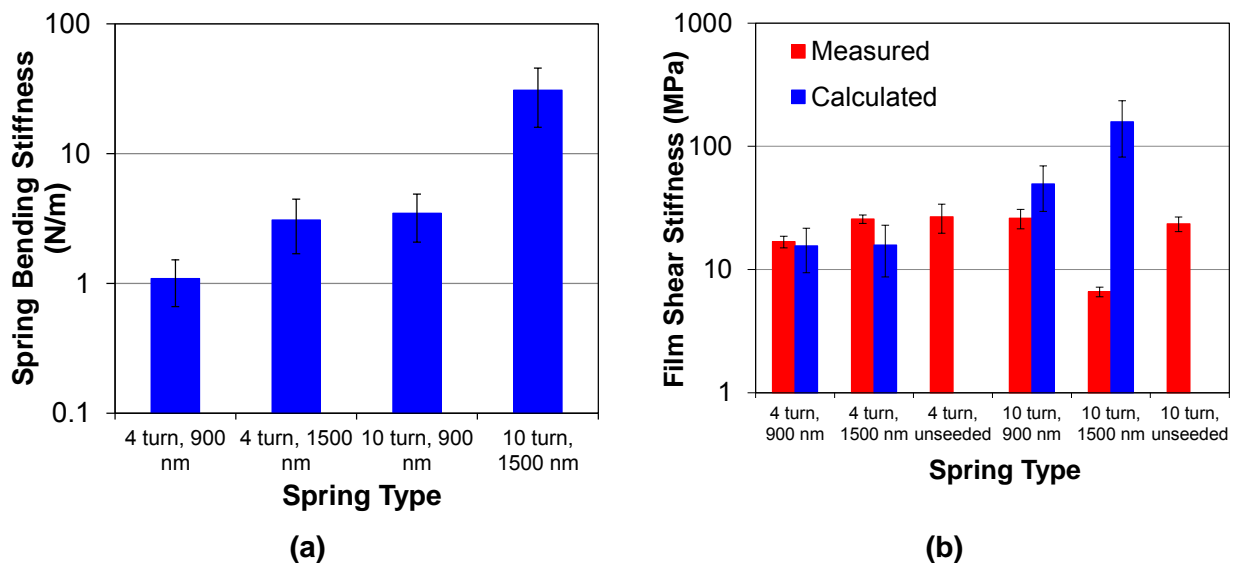
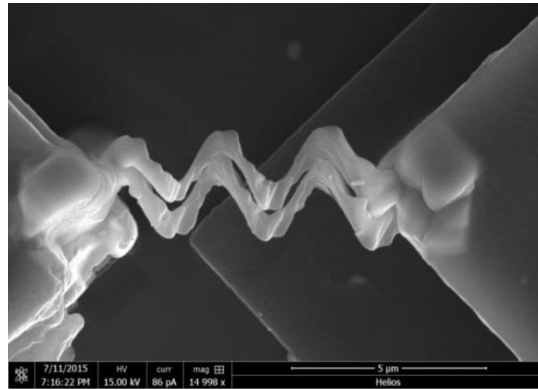


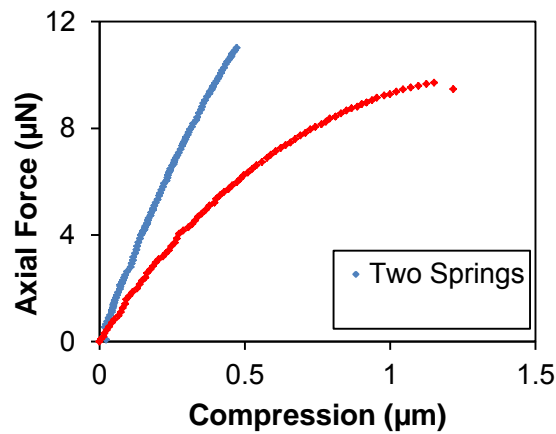
Figure 36. (a) Individual spring bending stiffness, and **(b)** film shear stiffness as measured and estimated from individual spring data. All individual spring stiffness values refer to 10- μm long springs. The logarithmic scale ensures that all results are shown properly in the same graph.

The effect of the lateral spring interactions with their neighbors on the axial and transverse stiffness was further investigated via experiments with two or more springs mounted on MEMS apparatuses. Figures 14(a) and 37(a) show an example of a pair of springs mounted for compression testing, and Figure 14(b) shows an example of a pair of springs mounted for testing in bending. A comparison of the force vs compression of two 4 turn springs with the curve for an individual 4-turn from the same film is shown in Figure 37(b). Similarly, the force vs. bending deflection of two 4-turn springs and a single 4-turn spring from the same film all subjected to bending loading is given in Figure 37(c). In compression the initial stiffness of the pair of two springs was 27 N/m, which is approximately twice the stiffness of a single spring. The graph for two 4-turn springs exhibited quite linear behavior compared to that of an individual spring, since the two springs mutually restricted each other from out-of-plane deflection. On the other hand, the force vs. bending deflection of two springs resulted in almost three times the bending stiffness of a single spring (4.8 N/m), while both curves were quite linear, Figure 37(c). Notably, both in compression and in bending the compressive or bending strength of a pair of

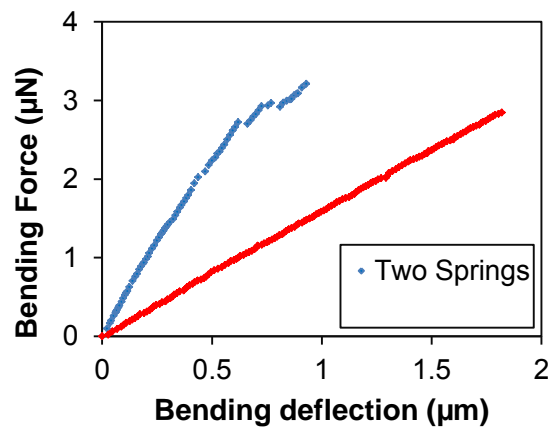
two springs was marginally larger than a single spring, plausibly because failure of one of the two springs shifted the entire load to the other (intact) spring that failed right after.



(a)



(b)



(c)

Figure 37. (a) A pair of springs mounted for compression testing. (b) Force vs. compression, and (c) force vs. bending deflection of a single and two 4-turn springs from a Si film with 900 nm seed spacing.

III.6 DISCUSSION

The results from the tension and compression experiments on individual Si springs were compared to analytical spring models by Wahl [39,40] and Ancker and Goodier [41,42]. The cross-section of the wire comprising each Si spring was approximated as elliptical upon imaging by SEM and Equations (4) and (7) were modified to take into account the elliptical cross-section. A comparison between experiments and modeling is shown in Figure 38. The experimentally determined compressive stiffness of individual springs deviated from the analytical predictions by the model of Wahl [39,40] by -15%, -10%, 72% and 392% and by the model of Ancker and Goodier [41,42] by -19%, 16%, 52% and 371% for springs from films with 4-turn coils and 900 nm seed spacing, 4-turn coils and 1500 nm seed spacing, 10-turn coils and 900 nm seed spacing, and 10-turn coils and 1500 nm seed spacing, respectively. Based on these results, the analytical model predictions are more accurate in predicting the compressive stiffness of 4-turn coils. However, the model predictions break down for the case of 10-turn coils which deviate from the open coil geometry that is used in the aforementioned analytical models. Similarly, the results for the tensile stiffness of individual Si springs deviated from analytical predictions by the model of Wahl [39,40] by 4%, -13%, 24% and 631% and by the model of Ancker and Goodier [39,40] by -1%, -19%, 9% and 601%, for springs from films with 4-turn coils and 900 nm seed spacing, 4-turn coils and 1500 nm seed spacing, 10-turn coils and 900 nm seed spacing, and 10-turn coils and 1500 nm seed spacing, respectively. Furthermore, there was good agreement between the experimental tension results and the predictions for 10-turn coils from films with 900 nm spacing. However, for those coils, the determination of the wire cross-section was not as clear and, therefore, any agreement is perhaps coincidental since the equations by Wahl [39,40] and Ancker and Goodier [41,42] were derived for open coils and the springs with 10-turn coils were closed coils.

The contribution of lateral spring interactions to the effective film stiffness could also be calculated by multiplying the initial stiffness of an individual spring with the area density of springs in films with different seed spacing. The number of springs included in the compression test areas was ~9070 for 900 nm seed spacing films and ~3265 for 1500 nm seed spacing. Furthermore, based on geometric considerations, the pressure required to achieve contact between neighboring springs in a film was estimated from SEM images as 4.9 MPa for films of 4-turn coils and 900 nm seed spacing, 4.7 MPa for films of 4-turn coils and 1500 nm seed spacing, 7.5 MPa for films of 10-turn coils with 900 nm seed spacing. Films comprised of 10-turn coils with 1500 nm seed spacing had no intertwining, Figure 3(d), therefore, were prone to titling or buckling. Figure 38 shows a comparison between the compressive film stiffness of capped and uncapped films at pressure levels 0.5 MPa, 5 MPa, and 10 MPa vs. the film stiffness estimated using the measured stiffness of individual Si springs as described above. Notably, the estimated compressive stiffness based on individual spring data (red bars in Figure 38) was in better agreement the stiffness of capped and uncapped Si films subjected to 10 MPa pressure. In general capped Si films were stiffer and in better agreement with single spring calculations, which is expected since springs in capped films approximated fixed-fixed boundary conditions, which was also the case for individual springs tested with MEMS devices. It is, thus, possible that not all springs in a film transfer load and a pressure as high as 10 MPa is required to engage all springs in a film.

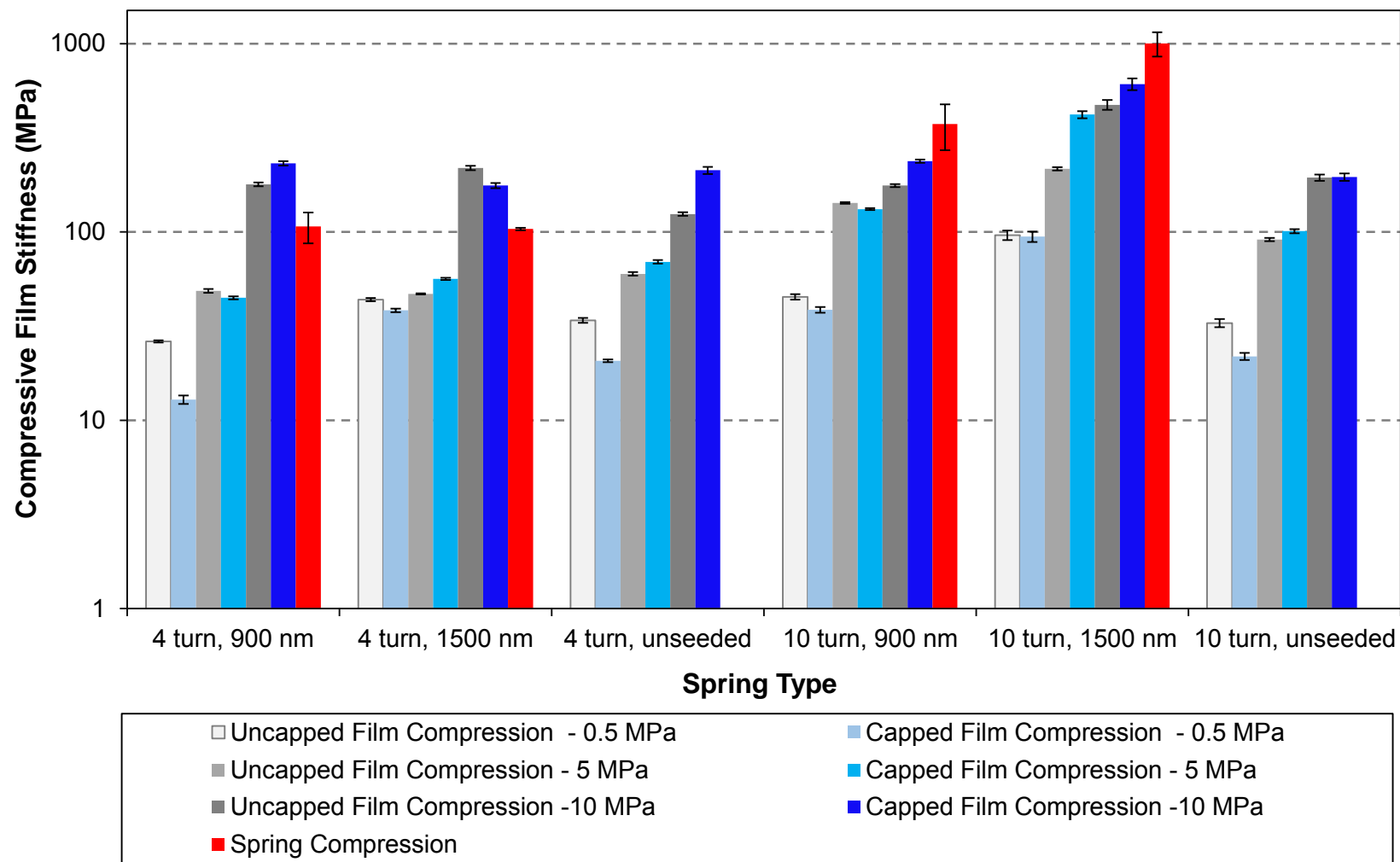


Figure 38. Comparison of the compressive stiffness of uncapped and capped Si films, subjected to 0.5 MPa, 5 MPa and 10 MPa, with the estimated film stiffness based on individual spring measurements (red bars).

IV. FUTURE PROSPECTS

IV.1.1. Improved Analysis and Design of GLAD Films

Current research at the PI's lab, sponsored by a recent and on-going AFOSR grant, focuses on understanding how the deposition parameters of the GLAD process affect the geometry and properties of individual springs and their films. As shown in Figure 39(left), unseeded spring growth results in dense springs with maximum interpenetration. As discussed in this report, although very dense, these films were more compliant than their seeded counterparts, e.g. Figure 39(right), unseeded films allow for limited customization of the compressive and shear films stiffness.

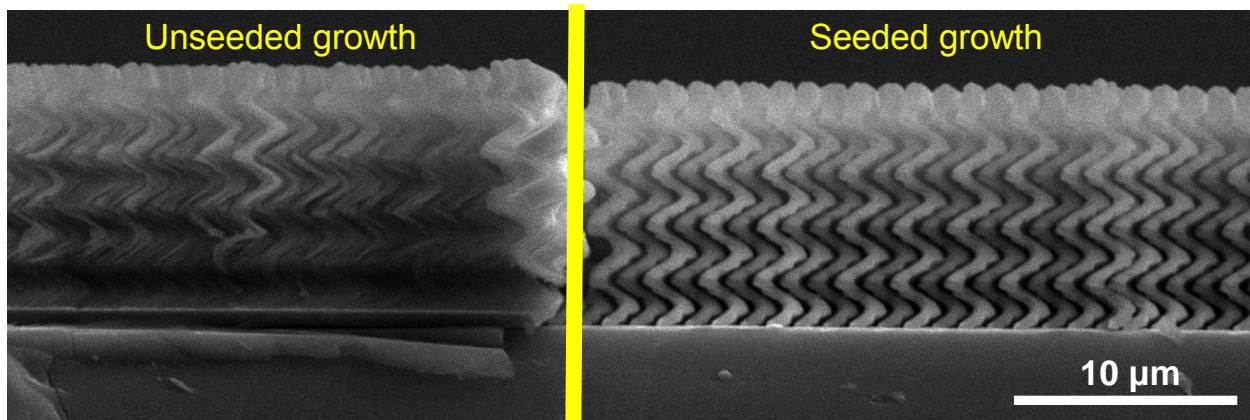


Figure 39. Left: Unseeded Si spring films. **Right:** Seeded Si springs with 4 coil turns.

Figure 40 shows a comparison of the geometry of an ideal coil and springs with 4 and 10 turns fabricated for the purposes of this research program: the results obtained in this research program for seeded, Figures 40(b,c), provided metrics about the relevance of springs from seeded films to ideal coils, Figure 40(a), which can be described by analytical models or finite element modeling. This information is invaluable in the design of spring films, and to assess the importance of spring interactions in films in relation to the effective film compressive and shear behavior. Important consideration in fabrication of GLAD springs that approximate ideal coils is the growth process which needs to be taken into account in the design of compliant interfaces comprised of nanosprings. An ongoing AFOSR-sponsored research program studies the details of GLAD process for the fabrication of compliant Cu spring films.

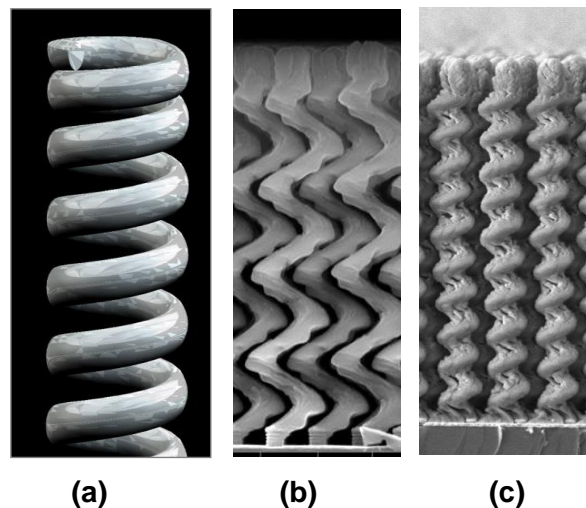


Figure 40. (a) Ideal spring, **(b)** 4-turn seeded Si spring, **(c)** 10-turn seeded Si spring.

IV.1.2. Multifunctional Films for Energy Storage

Si has very large theoretical Li^+ capacity, reaching 3,590 mAh/gr, in comparison to widely used graphite with gravimetric capacity of 372 mAh/gr [46]. However, Si exhibits large volumetric expansion (up to 300%) upon lithiation, resulting in fragmentation and delamination of thin film anodes [47]. The capacity fade of an anode depends on the thickness of a thin film, with thicker films (microns in thickness) exhibiting reduced capacity after a smaller number of electrochemical cycles compared to thinner films (tens to hundreds of nanometers in thickness). While a reduction in film thickness can avert performance degradation, very thin anodes are impractical in terms of total capacity. A solution could be provided by relatively thick anodes (tens of microns in thickness) comprised of dense arrays of nanostructures, which, due to their small dimensions are not prone to fracture due to lithiation [47] while can also lithiate fast.

Such arrays of nanocolumns have been developed before by different techniques [48-50], but they suffer from bending if both ends of those nanocolumns are fixed. Unfortunately, this bending is irreversible upon delithiation. Nanostructures that expand preferentially in the radial direction, such as springs, could provide a solution to this issue. This architecture for a Si anode has been demonstrated before with stable electrochemical cycling for more than 100 cycles [19,20,51]. Helical films exhibited better performance than films comprised of slanted columns due to better adhesion to the substrate and higher porosity and surface area, which accommodated Li^+ transport. Prior studies, however, did not investigate the dependence of chemical lithiation on the geometrical details of helical nanostructures.

Preliminary data were obtained in the course of this research program that demonstrated the potential of films comprised of Si helical structures. Different types of Si nanoparticles with various geometries were subjected in the past to *in-situ* chemical [52,53] and electrochemical [54,55] lithiation; following the procedures in these references we performed chemical lithiation of Si nanosprings. The results are discussed in the next Section. A collaboration with a computational group with expertise in electrochemical studies is currently in place aiming at a publication in the first half of 2017.

IV.1.3. In-Situ Lithiation of Columnar and Helical GLAD Structures

For this pilot study, Si columns were fabricated at Micralyne using GLAD with the substrate tilted at 85° while rotated at constant speed [11,12], which was at least an order of magnitude faster than the rotation speed for the fabrication of the spring films described earlier in this report.

Individual Si columns and springs were isolated from films and mounted with an adhesive at the tip of a probe. The test structures were brought to contact with Li metal via a nanomanipulator inside a FIB chamber. The surface of the Li metal forms Li_2O after short exposure to air. Once the Si columns or springs were in contact with the Li_2O surface, the electron-beam was focused near the contact point causing Li_2O break-down and release of elemental Li atoms which diffused into the Si columns and springs. Li_2O break-down took place for electron beam intensities larger than 50 A/m^2 , which was determined experimentally, in comparison to prior reports of $\sim 100 \text{ A/m}^2$ [52]. The test structures were subjected to pure chemical lithiation, which, compared to electrochemical lithiation, does not involve the

application of an electrical potential between the anode and the cathode [56]. The evolution of the geometry of the Si columns and springs during lithiation was monitored at regular time intervals. Figure 41(a,b) shows two examples of Si columns which were progressively lithiated until no more Li was possible to intercalate. The images show the progression in wire diameter change during lithiation, with evident asymmetric bending that was not relieved upon removal of the constrains at the wire ends. Lateral deformation of the Si nanocolumns occurred even when the probe holding the Si nanocolumn in Figure 41(b) was retreated periodically between steps of chemical lithiation, allowing for the compressive stress to be intermittently relieved.

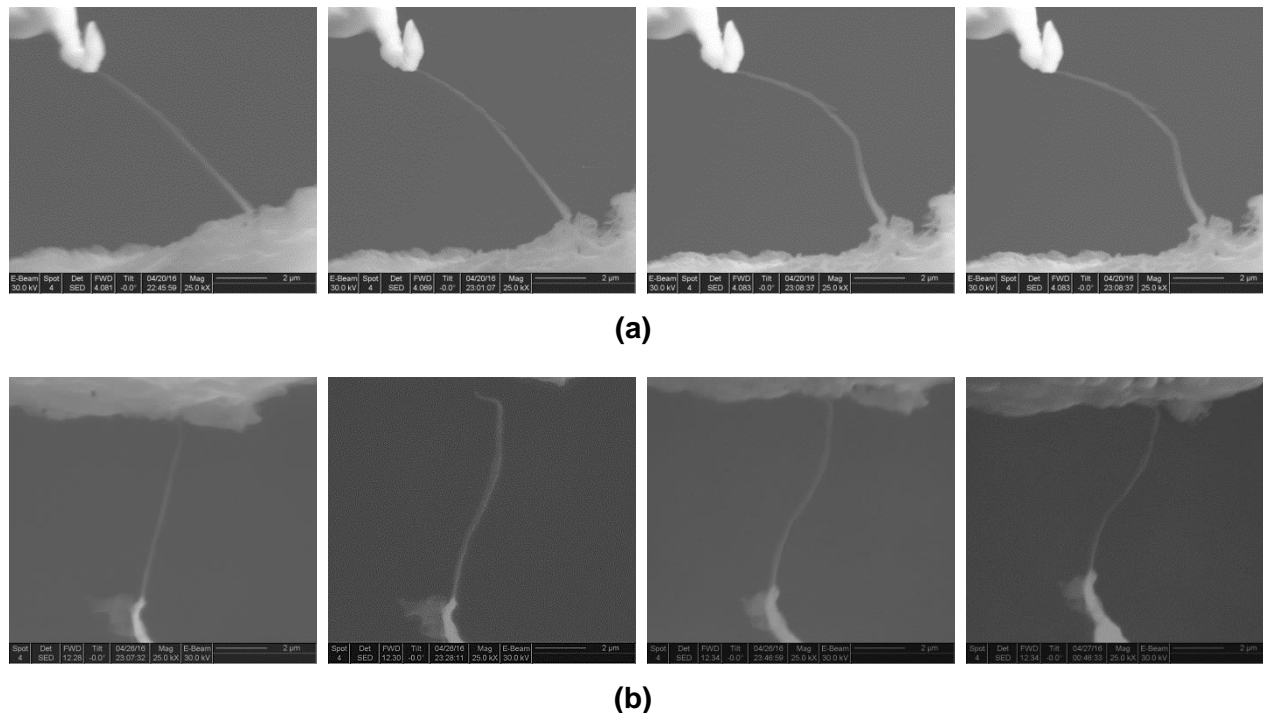
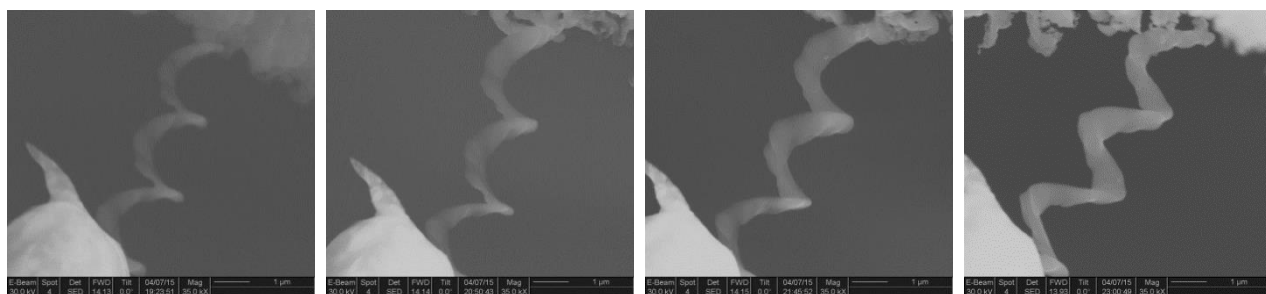
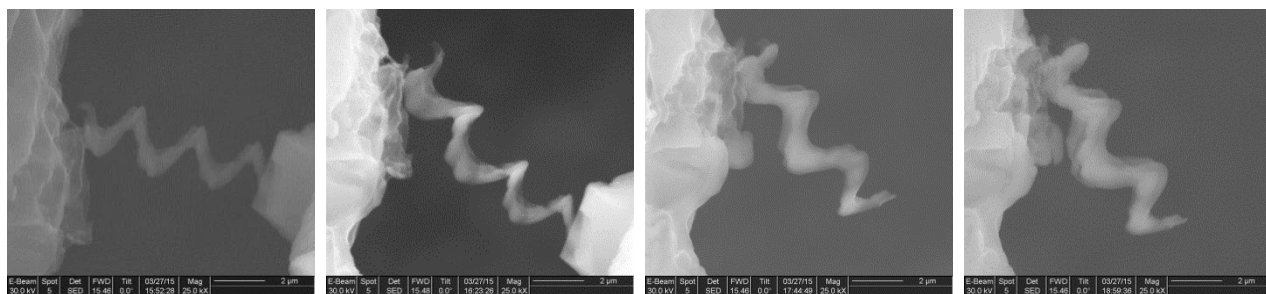


Figure 41. (a,b) In-situ chemical lithiation of two Si columns fabricated via GLAD.

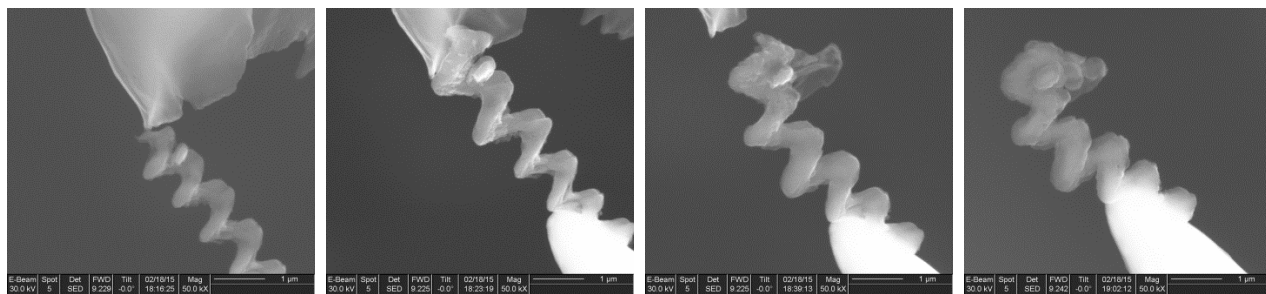
Similarly, chemical lithiation was conducted inside a FIB chamber to four types of Si springs, as shown in Figures 42(a-d), which were characterized by two different spring pitches and wire diameters. During lithiation, the Si springs expanded both in the radial and the longitudinal directions. Very limited cracking due to Li atom diffusion was evidenced by the single crack in the springs shown in Figures 42(b,d), which were the spring with larger wire diameters. Current research efforts focus on evaluating the volume increase in chemically lithiated columns and springs and relate time lapse data to computational modeling results. Time permitting, mechanical tests will be conducted with Si nanosprings or columns to assess their mechanical strength and stiffness upon chemical lithiation, in comparison to the mechanical measurements on pristine Si nanosprings reported in this Final Progress Report.



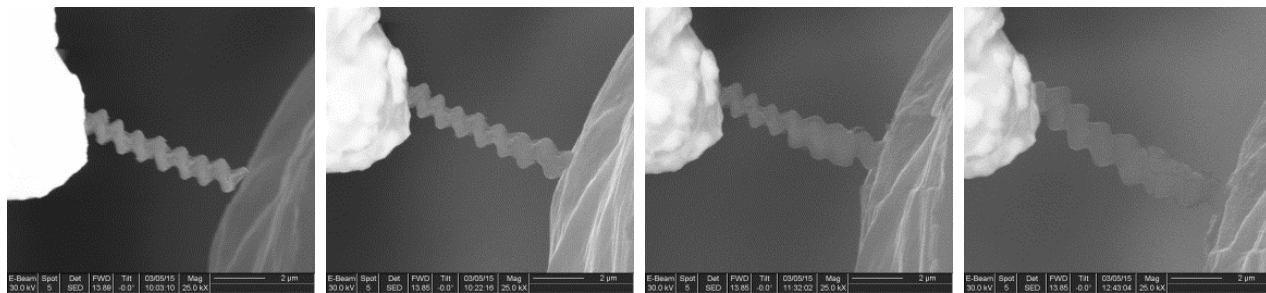
(a)



(b)



(c)



(d)

Figure 42. *In-situ* chemical lithiation of individual Si springs from films with **(a)** 4-turn coils and 900 nm seed spacing, **(b)** 4-turn coils and 1500 nm seed spacing, **(c)** 10-turn coils and 900 nm seed spacing, and **(d)** 10-turn coils and 1500 nm seed spacing.

V. REFERENCES

- [1] Kharisov BI, Krarissova OV, Garcia BO, Méndez YP and Gómez de la Fuente I, "State of the art of nanoforest structures and their applications", *RSC Advances*, 5, 2015, 105507-105523.
- [2] Qu L, Dai L, Stone M, Xia Z and Wang ZL, "Carbon nanotube arrays with strong shear binding-on and easy normal lifting-off", *Science*, 322, 2008, 238-242.
- [3] Ge L, Ci L, Goyal A, Shi R, Mahadevan L, Ajayan PM and Dhinojwala A, "Cooperative adhesion and friction of compliant nanohairs", *Nano Letters*, 10, 2010, 4509-4513.
- [4] Tong T, Zhao Y and Delzeit L, "Dense vertically aligned multiwalled carbon nanotube arrays as thermal interface materials", *IEEE transactions on components and packaging technologies*, 30, 2007, 92-100.
- [5] Kumar A, Maschmann MR, Hodson SL, Baur J and Fischer TS, "Carbon nanotube arrays decorated with multi-layer graphene-nanopetals enhance mechanical strength and durability", *Carbon*, 84, 2015, 236-245.
- [6] Sadasivam S, Hodson SL, Maschmann MR and Fischer TS, "Combined microstructure and heat transfer modeling of carbon nanotube thermal interface materials", *Journal of Heat Transfer*, 138, 2016, 042402-1-042402-12.
- [7] Chen X, Zhang S, Dikin DA, Ding W, Ruoff RS, Pan L and Nakayama Y, "Mechanics of a carbon nanocoil", *NanoLetters*, 3, 2003, 1299-1304.
- [8] Daraio C, Nesterenko VF, Jin S, Wang W and Rao AM, "Impact response by a foamlike forest of coiled carbon nanotubes", *Journal of Applied Physics*, 100, 2006, 063409-1-063409-4.
- [9] Coluci VR, Fonseca AF, Galvão DS and Daraio C, "Entanglement and the nonlinear behavior of forests of coiled carbon nanotubes", *Physical Review Letters*, 100, 2008, 086807-1-086807-4.
- [10] Shaddock D, Weaver S, Chasiotis I, Shah B and Zhong D, "Development of a compliant nanothermal interface material", *Proc ASME 2011*, 2011, 1-5.
- [11] Hawkeye M and Brett MJ, "Glancing angle deposition "Fabrication, properties, and applications of micro- and nanostructured thin films", *Journal of Vacuum Science and Technology A*, 25, 2007, 1317-1335.
- [12] Taschuk MT, Hawkeye MM, and Brett MJ. "Glancing Angle Deposition." *Handbook of Deposition Technologies for Films and Coatings*. 3rd ed. N.p.: Elsevier, n.d. 621-678. Print, 2010.
- [13] Zhao Y, Growth and synthesis of nanostructured thin films, *Integrated Analytical Systems*, 2009, 31-64.
- [14] Kesapragada SV and Gall D, "Anisotropic broadening of Cu nanorods during glancing angle deposition", *Applied Physics Letters*, 89, 2006, 203121-1-3.
- [15] Huang G and Mei Y, "Helices in micro-world: Materials, properties, and applications", *Journal of Materiomics*, 1, 2015, 296-306.
- [16] Barranco A, Borrás A, Gonzalez-Elipé AR and Palmero A, "Perspectives on oblique angle deposition of thin films: From fundamentals to devices", *Progress in Materials Science*, 76, 2016, 59-153.

- [17] Tounsi N, Barhoumi A, Chaffar Akkari F, Kanzari M, Guermazi H and Guermazi S, "Structural and optical characterization of copper oxide composite thin films elaborated by GLAD technique", *Vacuum*, 121, 2015, 9-17.
- [18] Malac M, Egerton RF, Brett MJ and Dick B, "Fabrication of submicrometer regular arrays of pillars and helices", *Journal of Vacuum Science & Technology B*, 17, 1999, 2671-2674.
- [19] Polat BD, Eryilmaz OL, Erck R, Keles O, Erdemir A and Amine K, "Structured SiCu thin films in LiB as anodes", *Thin Solid Films*, 572, 2014, 134-141.
- [20] Polat BD, Keles O and Amine K, "Silicon-copper helical arrays for new generation lithium ion batteries", *Nano Letters*, 2015.
- [21] Krishnan R, Lu TM and Koratkar N, "Functionally strain-graded nanoscoops for high power Li-ion battery anodes", *Nano Letters*, 11, 2011, 377-384.
- [22] Merkel JJ, Sontheimer T, Rech B and Becker C, "Directional growth and crystallization of silicon thin films prepared by electron-beam evaporation on oblique and textured surfaces", *Journal of Crystal Growth*, 367, 2013, 126-130.
- [23] Kintymer J, Martin N, Chappé JM, Delobelle P and Takadoum J, "Influence of zigzag microstructure on mechanical and electrical properties of chromium multilayered thin films", *Surface and Coatings Technology*, 180-181, 2004, 26-32.
- [24] Yildiz A, Cansizoglu H, Turkoz M, Abdulrahman R, Al-Hilo A, Cansizoglu MF, Demirkan TM and Karabacak T, "Glancing angle deposited Al-doped ZnO nanostructures with different structural and optical properties", *Thin Solid Films*, 589, 2015, 764-769.
- [25] Seto MW, Robbie K, Vick D, Brett MJ and Kuhn L, "Mechanical response of thin films with helical microstructures", *Journal of Vacuum Science and Technology*, 17, 1999, 2172-2177.
- [26] Seto MW, Dick B and Brett MJ, "Microsprings and microcantilevers: studies of mechanical response", *Journal of Micromechanics and Microengineering*, 11, 2001, 582-588.
- [27] Hirakata H, Matsumoto S, Takemura M, Suzuki M and Kitamura T, "Anisotropic deformation of thin films comprised of helical springs", *International Journal of Solids and Structures*, 44, 2007, 4030-4038.
- [28] Sumigawa T, Hirakata H, Takemura M, Matsumoto S, Suzuki M and Kitamura T, "Disappearance of stress singularity at interface edge due to nanostructured thin film", *Engineering Fracture Mechanics*, 75, 2008, 3073-3083.
- [29] Liu DL, Ye DX, Khan F, Tang F, Lim BK, Picu RC, Wang GC and Lu TM, "Mechanics of patterned helical Si springs on a Si substrate", *Journal of Nanoscience and Nanotechnology*, 3, 2006, 492-495.
- [30] Sneddon IN, "Boussinesq's problem for a flat-ended cylinder", *Mathematical Proceedings of the Cambridge Philosophical Society*, 1, 1946, 29-39.
- [31] Fischer-Cripps AC, "A review of analysis methods for sub-micron indentation testing", *Vacuum*, 58, 2000, 569-585.
- [32] Fischer-Cripps A, Introduction to contact mechanics, 2nd edition, Springer Science LLC, Inc. New York, pp.92-99. 2007.

- [33] VanLandingham MR, "Review of instrumented indentation", *Journal of Research of the National Institute of Standards and Technology*, 108, 2003, 249-265.
- [34] Oliver WC and Pharr GM, "An improved technique for determining hardness and elastic modulus using load and displacement sensing indentation experiments", *Journal of Materials Research Society*, 7, 1992, 1564-1583.
- [35] Naraghi M, Chasiotis I, Kahn H, Wen Y and Dzenis Y, "Mechanical deformation and failure of electrospun polyacrylonitrile nanofibers as a function of strain rate," *Applied Physics Letters*, 91, 2007, 151901.
- [36] Naraghi M, Chasiotis I, Kahn H, Wen Y and Dzenis YA, "Novel method for mechanical characterization of polymeric nanofibers", *Review of Scientific Instruments*, 78, 2007, 085108-1-8.
- [37] Naraghi M and Chasiotis I, "Optimization of comb-driven devices for mechanical testing of polymeric nanofibers subjected to large deformations", *Journal of Microelectromechanical Systems*, 18, 2009, 1032-1046.
- [38] Kolluru PV and Chasiotis I, "Interplay of molecular and specimen length scales in the large deformation mechanical behavior of polystyrene nanofibers", *Polymer*, 56, 2015, 507-515.
- [39] Wahl AM, Mechanical Springs, 1st edition, Penton Publishing Company, 1944, 62-68.
- [40] Wahl AM, Mechanical Springs, 2nd edition, McGraw-Hill, 1963.
- [41] Ancker CJ and Goodier JN, "Pitch and curvature corrections for helical springs", *Journal of Applied Mechanics*, 1958, 466-470.
- [42] Ancker CJ and Goodier JN, "Theory of pitch and curvature corrections for the helical springs – I (Tension)", *Journal of Applied Mechanics*, 1958, 471-483.
- [43] Zhang G and Zhao Y, "Mechanical characteristics of nanoscale springs", *Journal of Applied Physics*, 95, 2004, 267-271.
- [44] Timoshenko, S, Strength of Materials Part II: Advanced Theory and Problems, D. Van Nostrand Company, Inc. New York, pp.55-58, 310-311. 1940.
- [45] Lee CY, Zhuo HC and Hsu CW, "Lateral vibration of a composite stepped beam consisted of SMA helical spring based on equivalent Euler-Bernoulli beam theory", *Journal of Sound and Vibration*, 324, 2009, 179-193.
- [46] Mukhopadhyay A and Sheldon BW. Deformation and stress in electrode materials for Li-ion batteries, *Progress in Material Science*, 2014, 63, 58-116.
- [47] Marachi JP, Hepp AF and Kumta PN. High Capacity, Reversible Silicon Thin-Film Anodes for Lithium-Ion Batteries, *Electrochem. Solid-State Lett.* 2003, 6(9), A198-A201.
- [48] Teki R, Datta MK, Krishnan R, Parker TC, Lu TM, Kumta PN and Koratkar N. Nanostructured silicon anodes for lithium ion rechargeable batteries, *Small*, 2009, 5, 2236-2242.
- [49] Fleischauer MD, Li J and Brett MJ. Columnar thin films for three-dimensional microbatteries, *Journal of the electrochemical society*, 2009, 156, A33-A36.
- [50] Au M, He Y, Zhao Y, Ghassemi H, Yassar RS, Garcia-Diaz B and Adams T. Silicon and silicon-copper composite nanorods for anodes of Li-ion rechargeable batteries, *Journal of Power Sources*, 2011, 196, 9640-9647.

- [51] Wu XL, Liu Q, Guo YG and Song WG. Superior storage performance of carbon nanosprings as anode materials for lithium-ion batteries. *Electrochemistry Communications*, 2009, 11, 1468-1471.
- [52] Liu XH, Liu Y, Kushima A, Zhang S, Zhu T, Li J and Huang JY. In Situ TEM Experiment of Electrochemical Lithiation and Delithiation of Individual Nanostructures. *Advanced Energy Materials* 2012, 2(7), 722-741.
- [53] Seo JH, Chou CY, Tsai YH, Cho Y, Seong TY, Lee WJ, Cho MH, Ahn JP, Hwang GS and Choi IS. Ultrafast chemical lithiation of single crystalline nanowires: in situ characterization and first principles modeling. *RSC Adv* 2015, 5, 17438-17443.
- [54] McDowell MT, Lee SW, Harris JT, Korgel BA, Wang C, Nix WD and Cui Y, "In situ TEM of two-phase lithiation of amorphous silicon nanospheres", *NanoLetters*, 13, 2013, 758-764.
- [55] Gu M, Li Y, Hu S, Zhan X, Xu W, Thevuthasan S, Baer DR, Zhang JG, Liu J and Wang C, "In situ TEM study of lithiation behavior of silicon nanoparticles attached to and embedded in a carbon matrix", *ACS Nano*, 2012, 6, 8439-8447.
- [56] Liu XH, Fan , Yang H, Zhang S, Huang JY and Zhu T. Self limiting lithiation in silicon nanowires, *ACS Nano*, 2013, 7 (2), 1495-1503.

AFOSR Deliverables Submission Survey

Response ID:7518 Data

1.

Report Type

Final Report

Primary Contact Email

Contact email if there is a problem with the report.

chasioti@illinois.edu

Primary Contact Phone Number

Contact phone number if there is a problem with the report

217-714-2252

Organization / Institution name

University of Illinois at Urbana-Champaign

Grant/Contract Title

The full title of the funded effort.

Compliant Nanospring Interfaces

Grant/Contract Number

AFOSR assigned control number. It must begin with "FA9550" or "F49620" or "FA2386".

FA9550-13-1-0149

Principal Investigator Name

The full name of the principal investigator on the grant or contract.

Ioannis Chasiotis

Program Officer

The AFOSR Program Officer currently assigned to the award

Dr. Byung 'Les' Lee

Reporting Period Start Date

04/01/2013

Reporting Period End Date

09/30/2016

Abstract

This research program investigated the mechanics of thin films comprised of dense arrays of 10-micron high Cu and Si micro and nanosprings fabricated as multifunctional compliant interfaces via Glancing Angle Deposition (GLAD). The Cu spring films had 10 coil turns and were deposited with 2000 nm, 2400 nm, 2800 nm, or 3200 nm seed spacing on Si wafers as well as on unseeded Si substrates. Larger seed spacing resulted in Cu springs with larger coil diameter and larger wire thickness. Compression tests were conducted with stress amplitudes between 5 MPa and 50 MPa. At 5 MPa, the compressive stiffness of Cu films was between 184 ± 2 and 353 ± 15 MPa, with larger values corresponding to larger seed spacing. Notably, the Cu spring films showed no permanent deformation until 20 MPa, when they experienced only 2% permanent strain. The shear stiffness of Cu films was between 218 ± 37 and 322 ± 85 MPa with unseeded films being the most compliant. Seeding resulted in a weaker interface with the substrate, while unseeded Cu spring films had significant shear strength averaging 16 ± 0.9 MPa. The normal and shear stiffness values of Cu spring films were several orders of magnitude smaller than bulk Cu and they could be designed to be independent of each other, as opposed to bulk Cu.

Similarly, 10-micron thick Si films comprised of individual springs with 4 or 10 coil turns and seed spacings

DISTRIBUTION A: Distribution approved for public release.

of 900 nm or 1500 nm were subjected to tension/compression and shear. At 0.5 MPa normal stress, the Si films had compressive stiffness between 26 ± 0.4 and 44 ± 0.9 MPa, while the permanent strain was at most 6.5%. Compared to seeded films, unseeded films had quite reduced compressive stiffness but equivalent or higher shear stiffness. The shear stiffness of the various types of Si spring films was between 7 ± 0.6 and 27 ± 7 MPa, namely ~ 4 orders of magnitude smaller than solid Si. Microscale uniaxial tension/compression and bending tests of individual Si springs, carried out with a MEMS-based apparatus, provided the properties of individual springs: Springs with 4 coil turns, which had the closest resemblance to ideal open coils, exhibited the smallest axial stiffness values, between 10 and 35 N/m, and the best agreement between film-level stiffness measurements and estimates for the film stiffness based on individual spring stiffness data.

Distribution Statement

This is block 12 on the SF298 form.

Distribution A - Approved for Public Release

Explanation for Distribution Statement

If this is not approved for public release, please provide a short explanation. E.g., contains proprietary information.

SF298 Form

Please attach your [SF298](#) form. A blank SF298 can be found [here](#). Please do not password protect or secure the PDF. The maximum file size for an SF298 is 50MB.

[SF298.pdf](#)

Upload the Report Document. File must be a PDF. Please do not password protect or secure the PDF. The maximum file size for the Report Document is 50MB.

[FinalReport.pdf](#)

Upload a Report Document, if any. The maximum file size for the Report Document is 50MB.

Archival Publications (published) during reporting period:

- D. Antartis, R. Mott, D. Shaddock, I. Chasiotis, "Multifunctional Films of Helical Cu Wires", to be submitted to Advanced Materials, 2017.
- D. Antartis, R. Mott, K-K, Hung, I. Chasiotis, "Compliant Interfaces of Helical Si Coils", to be submitted to Small, 2017.
- D. Antartis, H. Wang, K-K, Hung, H.B. Chew, I. Chasiotis, "Lithiation Studies of Columnar and Helical Si Nanostructures", to be submitted to Experimental Mechanics, 2017.

New discoveries, inventions, or patent disclosures:

Do you have any discoveries, inventions, or patent disclosures to report for this period?

No

Please describe and include any notable dates

Do you plan to pursue a claim for personal or organizational intellectual property?

Changes in research objectives (if any):

N/A

Change in AFOSR Program Officer, if any:

N/A

Extensions granted or milestones slipped, if any:

A 6-month no cost extension was granted to complete the planned research.

AFOSR LRIR Number

LRIR Title

Reporting Period

DISTRIBUTION A: Distribution approved for public release.

Laboratory Task Manager

Program Officer

Research Objectives

Technical Summary

Funding Summary by Cost Category (by FY, \$K)

	Starting FY	FY+1	FY+2
Salary			
Equipment/Facilities			
Supplies			
Total			

Report Document

Report Document - Text Analysis

Report Document - Text Analysis

Appendix Documents

2. Thank You

E-mail user

Jan 22, 2017 15:05:38 Success: Email Sent to: chasioti@illinois.edu